Chapter 2

Nanolithography with an Atomic Force Microscope

Nano-features on surfaces are of increasing importance for the development of new device technologies. The knowledge of local oxidation mechanisms and kinetics is of crucial importance for optimizing the oxidation process by means of Scanning Probe Microscopes (SPMs), particularly, Atomic Force Microscope (AFM). AFM nanooxidation is used in the fabrication of electron devices with feature sizes as small as tens of nanometers. Also, an understanding of the local oxidation mechanisms and kinetics would provide the reliable control of the device performance.

In this chapter, nanometer-scale oxide patterns were fabricated on p-GaAs(100) surface by using an AFM-based anodic oxidation technique with a conductive tip and/ a carbon nanotube tip. The application of a negative to an AFM tip relative to

the sample substrate permitted nanometer-scale dots, wires and bumps of GaAs-oxides to be fabricated directly on GaAs surface. Studies on growth kinetics reveal that the nanostructure composition and their formation mechanism are the electric field /and relative humidity-dependent. The size dependence of the modified oxide structures on the oxidation parameters is studied in detail and, the elemental analysis of the modified structures is also performed using Auger Electron Spectroscopy (AES).

Furthermore, AFM-based nanoindentation technique was carried out on anodized structures for determining their nanohardness values. And, the nonlinear I-V curves showed that electronic flow across the GaAs oxide nanodot which follows the Fowler-Nordheim (FN) tunneling mechanisms over a range of applied bias. Results show that AFM tip-induced nanooxidation is to be a promising method for fabricating GaAs and, the effort to integrate AFM-based fabrication, electrical and mechanical characteristics in terms of the development of a physical model for the optimizations of the fabrication process and possible choices of future AFM-based nanodevices was studied and documented in this chapter.

Part of this chapter has been published and submitted in:
1.) S.R. Jian, T.H. Fang and D.S. Chuu, ***J. Phys. D: Appl. Phys.*** 38 (2005) 2424;
2.) S.R. Jian, W.P. Huang, C.M. Lin, J.Y. Hsieh, D.S. Chuu and H.H. Cheng, *submit* to ***Nanotechnology*** (2006).

2.1 Tip-induced local anodic oxidation mechanisms

From the pioneering work of Dagata *et al*. [1] demonstrating the tip–induced local oxidation of H-passivated Si(111) surface using a *Scanning Tunneling Microscope* (STM) in an ambient way, SPM-based local oxidation technique has been attracting increasing interest for its capabilities of nanometer-scale pattern formation and promising applications in nanodevices fabrication [2-9]. In Ref.1, it was shown that electrical and structural properties of the positive-based surface are changed irreversibly at room temperature under the tip effect. The common explanation of these changes is oxide formation. The dependences of the oxide pattern shape and growth kinetics on the conditions of tip-induced treatment obtained in various works allow us to propose an electrochemistry mechanism of nanooxidation. The process of local oxidation of a metallic or semiconducting surface induced by SPM tips is analogous to electrochemical anodic oxidation. In this system, the tip and the sample surface act as the cathode and anode, respectively, and the water meniscus condensed between the tip and the sample surface from the ambient humidity is the electrolyte. As a negative bias is applied to the tip, the OH^- ions contained in the water meniscus are driven to the sample surface by the electric field and localized anodic oxidation of the sample occurs beneath the tip apex, resulting in the growth of oxide structures with the width of 10–100nm and height of 1–10nm. In Ref.10, Snow *et al*. reported that the fabrication of an etching mask on the H-passivated Si surface with an AFM and achieved structures with a depth of 10nm in a subsequent etching process. Moreover, Shirakashi *et al*. [11] reported the observation of single electron effect at room temperature with a tunneling junction fabricated on the Nb surface by an AFM tip-induced local oxidation technique.

Even if an STM was first used with this technique, its main shortcoming is the

convolution of the topographic and the electronic information of the imaged structures, raising a difficulty in identifying the precise height of oxide patterns in the subsequent imaging on the surface. In contrast, an alternate approach making use of an AFM with a conductive tip negatively biased with respect to sample surface, proved to be more preferable. On the other hand, for the case of an AFM, a tip bias can be independently applied during the tip-induced nanofabrication processes without changing the tip-sample distance, because the tip-sample distance in an AFM is controlled by maintaining a constant force, rather than a constant current in a STM. Hence, an AFM can be used for nanofabrication on an insulating, as well as the conducting surfaces. Because of this additional advantage compared with a STM, the major focus has been on nanofabrication via the use of an AFM. Although this technique is an efficient method for fabricating nanometer-scale structures that can not be achieved by conventional lithography techniques, further improvement of the resolution and reliability of this technique is highly required for the fabrication of ultra-fine structures and novel nanodevices. Nevertheless, this remains a great challenge because the mechanisms and dynamics of the process of tip-induced local oxidation are still under study.

For optimal AFM anodization processing of nanodevices, it is essential to understand the mechanisms and kinetics of the process so that the diagnostics can be reliably controlled. In this chapter, AFM tip-induced local anodic oxidation on *p*-GaAs(100) surface which is operated in non-contact mode (ncAFM) is presented in an ambient way. Our studies are focused on the relationship between geometrical characters and exposure parameters, in order to determine how these parameters affect the growth of the oxides and how to improve the resolution and controllability of fabricated structures by controlling these parameters and, the elemental analysis of the modified structures is also performed by using AES.

The understanding of the AFM tip-induced surface properties, especially its current-voltage (*I-V*) characteristics, is a major issue for the usage as insulator films of nanodevices. As well, the *I-V* electrical characterization at room temperature of before and after the fabrication of GaAs oxides was investigated.

2.1-1 Scanning probe oxidation by Non-contact AFM

To date, several AFM modes (including contact [12], tapping [13] and non-contact (nc) [14]) have been applied to perform local oxidation lithography. During the oxidation, there is a strong interaction between the tip and surface and thus, the problem of the reliability of this approach is faced. In the case of ncAFM, a step towards a better reliability with respect to contact mode is made because the tip is in weak interaction with the surface. In addition, ncAFM oxidation allows controlling the lateral dimensions and exhibits higher aspect ratio (height/width) for performing local oxidation lithography [15].

§ Experiment details — In this present work, nanolithography is performed by using a commercial AFM (CP-R SPM, Veeco/TM, USA) and lithography software for non-contact dynamic mode to perform the oxidation experiments. A Pt-coated probe tip with a silicon cantilever was used. The curvature radius of the tip is 35nm. The force constant and resonance frequency of the non-contact mode cantilevers used are 34N/m and 350kHz, respectively. The sample is *p*-GaAs(100) with a resistivity of 10Ωcm, with a root-mean-square surface roughness of less than 0.2nm and an average surface roughness of less than 0.3nm. Before the lithography is performed on GaAs surface, an area is scanned and the plane is stored. Then the feedback loop is switched off during the lithography process. After the lithography has been performed

the feedback loop is activated and the same area is scanned again revealing the anodized structure. AFM set point value is presented as the current representing the deflection of the cantilever, which is proportional to the strength of tip-sample interaction. In order to compare the geometrical size of patterns formed at different exposure conditions, a very stable conductive tip was required to avoid the errors caused by tip degradation under the applied voltages. The cantilever was exercised at its resonance frequency, and the vibrational amplitude was approximately 16–20nm (peak to peak) during scanning. During regular scanning operation the tip-sample distance (*d*) is approximately 10nm, corresponding to tapping and total non-contact mode. Further description of the dynamic parameters needed to operate the AFM in a non-contact mode can be found elsewhere [16-18]. All experiments reported here were performed which the same tip to maintain the comparability of the results obtained with different exposure parameters. All records were performed three times and finally averages of three times oxidation tests were taken and the error estimation is approximately within 10–30%. As well, for environmental control, the microscope was placed into a closed box with inlets for dry and H_2O-saturated nitrogen. A digital hygroscope was used to monitor the humidity around the tip region and, wet or dry nitrogen was introduced into the cover of the SPM head to keep the relative humidity constant at values ranging from 50% to 80% with an accuracy of 1% by a humidity regulator during AFM nanooxidation.

AFM lithography is an electrochemical process characterized by the following brief description. When an AFM tip is brought to a sample surface in air or a humid atmosphere, a water bridge is formed around the tip-sample junction due to the capillary force of the adsorbed water. Directly evidence for the presence of water film has been reported in Ref.4. Thus, the electrochemical reactions would be expected to

be induced at the tip/water and sample/water interface as an appropriate bias voltage is applied between the tip and the sample. This process is strongly dependent upon three factors as follow: 1.) the formation of the water meniscus between the tip and sample surface (i.e. the humidity and tip-sample distance) and 2.) the creation of a field of sufficient strength to ionize the water meniscus and 3.) the duration of the application of that field. Fig.2-1 schematically depicts the mechanism used in this work for forming nanooxidation structures. In this technique, AFM tip acts as a cathodically biased electrode to the sample surface, while an adsorbed water layer on the sample surface dissociates due to a high electric field and acts as an electrolyte producing this electrochemical reaction. Oxyanions (OH^- and O^-) contribute to the formation of surface oxides and, because of diffusion through the oxide layer, also to the growth of oxides underneath. This process strongly depends on the amount of adsorbed water and, the water bridge size is increased as the anodized voltage or time increases. More description of the size of field-induced water bridge in ncAFM can be found elsewhere [19-20]. By scanning an AFM tip, GaAs-oxides structures were formed. Therefore, the chemical reactions and charge transfer processes have to be considered while analyzing the kinetics of *p*-GaAs(100) anodic oxidation are described as following:

Reactions at p-GaAs(100) surface

$$2GaAs + 6H_2O + 12h_{hole}^+ \rightarrow Ga_2O_3 + As_2O_3 + 12H^+ \quad (1)$$

$$6H_2O + 12h_{hole}^+ \rightarrow 3O_2 \uparrow + 12H^+ \quad (2)$$

Reaction at an AFM tip

$$12H_2O + 12e^- \rightarrow 6H_2 \uparrow + 12OH^- \quad (3)$$

Reaction in water

$$12H^+ + 12OH^- \rightarrow 6H_2O \quad (4)$$

In the case of nanooxidation, therefore, it can be expected that the H^+ and OH^--ions generated by reactions (1)–(3) will recombine immediately according to the recombination reaction (4). Here, h_{hole}^+ denotes positively charged holes on the *p*-GaAs(100) surface [21].

2.1-2 AFM oxidation kinetics of GaAs surface

To optimize the feature size, experiments were performed to determine the oxidation kinetics. Dots of different sizes were formed by the applications of pulses of identical voltages but different duration. An estimation of the growth rate was obtained by calculating the ratio between the dot height and the time the pulse was applied.

§ Effect of the amplitude and duration of static voltages

Fig.2-2(a) depicts a sequence of AFM imaged oxide dots fabricated using the ncAFM-based oxidation method. The patterns in Fig.2-2(a) row 1 were obtained by using a constant voltage of 10V at the different oxidation times of 10, 5, 2 and 1s. The patterns in Fig.2-2(a) row 2 were obtained by using a constant oxidation time of 5s using the different anodization voltages of 7, 8, 9 and 10V. These experiments were carried out in an environment having 60% relative humidity. The height profiles for row 1 and row 2 lines are shown in Fig.2-2(b). It is found that a longer anodization time and a larger anodization voltage results in larger and higher oxidized dots. This implies that the oxide dots not only grow along the vertical direction but also along the horizontal direction. Figs.2-3(a)&(b) represent the oxide height, the aspect ratio and oxide volume as a function of the anodization time at the four anodization voltages (7–10V). It can be seen that the oxide height, oxide volume and aspect ratio

increase as the logarithm of the anodization time increases and when the anodization voltage is increased. To pattern a dot for a given size the anodization times should be shorter or longer in relationship to the corresponding anodization voltages which would be higher or lower, respectively. In the insert of Fig.2-3(a), it was clear that the aspect ratio of *p*-GaAs(100) oxides could be improved using an anodized voltage, implying the enhancement of oxidation by an electric field.

In this experiment, the curvature radius of the tip used is about 3.5 times larger than *d* value, then the electrical field strength on the sample surface and underneath the tip can be approximated by $E = V / h$ (With constant anodic potential *V*, the strength of field in oxide falls as anodic oxide is grown and, therefore, electronic field is in inverse proportion to the height of grown oxide, *h*). Oxide dots of different sizes were performed by the application of anodization voltages but different anodization times. An estimation of the growth rate was obtained by calculating the ratio between the dot height and the time was applied. As a consequence, the growth rate decreases exponentially with the height of the oxide (please see Fig.2-4(b)) and follows the equation as pointed out by Avouris *et al.* [4]:

$$\frac{dh}{dt} \propto \exp(-\frac{h}{l_c}) \tag{5}$$

where *h* is the oxide height at time *t*, and l_c is a characteristic length depending on the anodization voltage.

Advanced by investigating the oxidation kinetics, the patterned oxide dots were fabricated and analyzed in Fig.2-2(a), and Fig.2-3(a) where no clearly threshold bias was observed. From Fig.2-3(a), we can estimate the oxide height to which the electrochemical process is diffusion limited at ~6nm, and can obtain the growth rate as a function of electronic strength as shown in Fig.2-4(a). In Fig.2-4(a) it can be seen that the growth rate increases as the electric field strength and applied anodization

voltages are increased. The initial growth rate is at the order of ~300nm/s for 10V, it decreases rapidly as the electric field strength is decreased. In addition, it was found that the anodization process is enhanced when the electric field strength is at an order of $2–3\times10^{7}$V/cm. It is also clear from Fig.2-4(a) that the growth rate is not only a function of electric field strength but also depends on the applied voltage. In addition, Fig.2-4(b) displays the relationships between the growth rate and the oxide height at four different applied bias voltages. The characteristic decay length is within the range of 0.45–0.71nm at the applied anodization voltages of 7–10V. Thus, as the oxides height grows, the electric field becomes weaker and accordingly the growth rate decreases. Although, the applied anodization voltage is increased, the growth rate becomes faster and the characteristic length is increased when the oxides height reaches its maximum for each time.

As mentioned above, the applied tip bias extends the electric field strength assisting the oxidation mechanisms until the growth is limited by the diffusion. Not only is the oxide rate a function of electric field strength but it also appears to depend on the bias voltage applied to the tip. The Cabrera-Mott theory [22] of field-induced oxidation cannot account for this observed kinetics. The differences between the kinetics of AFM nanooxidation and the Cabrera-Mott field model have been attributed to such mechanism as follows: 1.) the mechanical stress created and arisen within the oxide nanodots because of a large volume mismatch between the sample and the oxides [23], and 2.) the space charge build-up within the oxide nanodots [24].

Previously [4] reported results on the development of the mechanical stress, arising during anodization, are due to a large volume mismatch in Si and SiO_2. The mechanical stress leads to additional activation energy, resulting in a rapidly decrease in the growth rate while the oxide height increases rapidly. Similar results can also account for the AFM-induced oxidation in GaAs film [23], due to the fact that the

volume of (Ga_2O_3 + As_2O_3) oxides are ~2.7–3.5 times larger than that of GaAs and the SiO_2 oxides are 2 times larger than that of Si. Consequently, the mechanical stress of the oxides/GaAs interface is larger than the oxides/Si interface. An applied anodized voltage of 10V causes the initial growth rate of the GaAs-oxide dot to be 300nm/s which is larger than the Si oxide dot which has a growth rate of 10nm/s [4]. In addition to that the value of growth rate of the AFM-generated oxide lines on *n*-GaAs(100) surface in Ref.23 (about 50nm/s at 10V) is smaller than our results. If the applied bias voltages are the same, then the faster the scan speed is performed the smaller the oxide structure is obtained. This implies that the lower growth rate can be found in oxide line structure. On the other hand, according to Ref.25, Teuschler *et al*. proposed that the *p*-Si(111):H has the higher oxide height than that of *n*-type at a particular bias voltage as well as a higher growth rate. Thereby, we can speculate that the difference is reasonably explained by the differently doped substrates, oxide structures and operational conditions (such as AFM-operated mode, the humidity and etc).

The ncAFM locally anodization was subjected to varying anodization voltages in the 7–10V range; the diffusion limited electric field strength corresponding to the oxide height of ~6nm is $2–3\times10^7$V/cm. This model accounted for the self-limiting growth, which was proposed by Stiévenard *et al*. [26]. The growth rate of anodized surface is governed by the ionic transportation that is promoted by the electric field strength. A greater height of the oxide protrusion corresponds to a weaker electrical field strength, which also limits oxide point growth. Thereby the AFM-based nanooxidation process has a self-limiting behavior resulting in a high initial oxidation rate, which decays exponentially and, reducing the electric field strength while there is a simultaneous rapidly build-up of the space charge.

§ *Effect of the relative humidity*

The dependency of the oxide height, the aspect ratio and oxide volume as a function of the anodization voltage at various relative humidity levels are plotted in Figs.2-5(a)&(b). It can be observed that the oxide height, oxide volume and aspect ratio increase as the relative humidity is increased, with the maximum size being formed at a relative humidity of 80%. Note that from the insert of Fig.2-5(a), there is no significant dependence of the aspect ratio on the humidity. The anodized oxide structure with a lower spatial resolution is obtained in higher relative humidity, so that the resolution becomes worse as the relative humidity is increased [27].

Sugimura *et al*. [28] proposed that the oxidation process is humidity dependent, leading towards an interpretation of the process in term of anodization, with the water acting as the electrolyte. Hence, the water bridge is very important because it plays an essential component in the formation of the oxides. The relative humidity around the AFM tip and the sample surface affects the oxides shapes as shown in the insert of Fig.2-6 and, in previous studies [4, 29-30]. At high relative humidity, the size and shape of the oxide dots are obviously changed by virtue of the contribution of ion diffusion to the anodization process on *p*-Si(001) surface, as reported in Ref.29. Drawing inspiration from the previous studies, we also performed and discussed the process on *p*-GaAs(100) surface and found that the same phenomenon occurred at high relative humidity (over 60%) also.

Fig.2-6 illustrates the width of oxide dots patterned at different anodization times. It can be seen that the relative humidity dominates the lateral diffusion process as the anodization time progresses. Also, it has been proved that the water meniscus between the tip and sample surface is necessary for the SPM-based local oxidation and its size is dependent on the ambient humidity [31]. When the relative humidity is increased, a greater thickness of water meniscus forms around the tip-sample junction (please see

the insert of Fig.2-6); also, the amount of oxyanions being migrated by an electric field in the lateral direction is increased. That is, the water meniscus will become wider as the humidity increases, and hence increases the quantity of OH^- ions contained within it, resulting in a significant enhancement of the growth in the width of the induced oxides. At an anodized voltage of 10V for 100s, the anodized area is broadened from 108nm in width to 142nm at the relative humidity of 50% and 80%, respectively. This process strongly depends on the amount of water available to be adsorbed, since the thicker water meniscus the higher humidity is and, correspondingly, the sample surface becomes anodized over a wider area [30-31].

Further recognizing of the nanooxidation process can be obtained by measuring the Faradaic current [32], since the transport of oxyanions between the AFM tip and the sample surface is ultimately responsible for the anodization process. High humidity promotes the contribution of ionic diffusion through surface water layer and decreases the Faradaic current. In terms of this, it can be concluded that the Faradic current causes significant lateral ionic diffusion that produces a wider anodized area. Based on this point of view, we assume that a local diffusion coefficient of OH^- ion [33] in the solid-liquid interface is about $D = 10^{-9}\text{cm}^2/\text{s}$ and the average displacement traveled by an ion is given by $r \sim \sqrt{Dt}$. In our case for t = 0.01s, r~32nm is approximately the experimental width. However, the experimental width cannot be expected to grow up to the theoretical value of ~3200nm at 100s because of the space charge build-up which arrested the lateral growth behavior. As revealed in Fig.2-4(a), the anodization process is limited as a result of the space charge accumulation at oxides/GaAs interface, as described above.

As shown in the above analysis, the change in the oxide volume is obviously greater at the higher anodization voltage and the relative humidity at longer

anodization time and, this implies that the continuation of oxidation is due to the contribution of ionic diffusion [29]. The contribution of ionic diffusion [29] to the AFM anodization process and an oxide dot with a “two-storied” shape (the parts of narrow upper and broad base) are illustrated in Fig.2-7(a), which are caused by the space charge effect and lateral ionic diffusion. At longer anodization times, the ion diffusion at 8V goes up to about 70% and at 10V goes up to about 80% while it remains below 30% when the anodization time is shorter even though the relative humidity is higher, please see the Fig.2-7(b). The ion diffusion phenomenon thus occurs at a longer anodization time and a higher anodized voltage. When comparing of the contribution of ionic diffusion between GaAs and Si, it was found that GaAs had a higher contribution of ionic diffusion than Si owing to a higher growth rate.

In closing, AFM tip-induced nanooxidation process is dependent on the electric field and the relative humidity. As the relative humidity increases, the spatial extent of the water meniscus also increases, which influences the process along with the applied bias voltage [29] because it determines the amount of adsorbed water layer and the primary source of oxyanions in the electrochemical reaction. Oxyanions are produced by the hydrolysis of the water within the meniscus. Such ions transport across the anodic oxide is strongly accelerated by an intense electric field produced in the oxide by the applied bias voltage. In this electrochemistry reaction, the high electrical field of the AFM tip produces oxyanions in the relative humidity that forms Ga(As)-O bonds on the surface.

2.1-3 micro-Auger analysis

In order to investigate the chemical composition of the locally anodized structures, *Auger electron spectroscopy* (AES, Auger 670 PHI Xi, Physical Electronics, U.S.A.) system equipped with a Schottky field emission electron source was used.

The electrochemical reaction causes local oxidation at *p*-GaAs(100) surface, that is, the electrical field drives OH^- ions in the water bridge to GaAs surface resulting in formation of the oxides. To provide the proof of that, AES analysis was conducted on an anodized area of $10\times10\mu m^2$ (~5nm oxide height). This region was made by ncAFM operated with 1μm/s scan speed and +10V bias applied to the sample. In Fig.2-8, AES records taken from the as-growth and modified areas are illustrated. Both spectra have emission peaks of Ga-*LMM* at ~1065eV and As-*LMM* at ~1225eV. Obviously, we can see the emission peak of O-*KLL* Auger electrons having the kinetic energy of ~512eV in Fig.2-8(b). Meanwhile, the magnitude of O-*KLL* is much enhanced on the anodized region as compared to that of the as-grown region, which suggests higher oxygen content in the modified area. The AES results support the suggestion of the previous study that the heavily C-doped GaAs film can be converted to oxides by local oxidation process [34] — the mobile oxyanions drift toward the anodic sample in response to the local electrical field beneath an AFM tip and react with *p*-GaAs(100) surface at the oxides/GaAs interface. In addition, *X-ray Photoelectron Spectroscopy* (XPS) is also a powerful technique for analyzing surface chemistry and composition. In the previous study [35], the chemical analysis of AFM tip-induced n^+-GaAs(100) oxides had also revealed that the main constituents are determined to be Ga_2O_3 and As_2O_3 by means of scanning microprobe XPS measurements. As a result of AES and XPS analysis, the products are shown to be GaAs oxides in a qualitative analysis briefly.

2.2 Nanohardness of oxide structures

If these GaAs-oxide structures is used at very light loads such as effect tunnel barriers for carrier transport in device applications, the high hardness of anodized nanostructure would protect the device until it is worn-out. Thus, the mechanical property of the anodized oxides should be recognized.

§ Experiment details — The nanoindentation results were performed on these oxide structures using the AFM nanoindentation system equipped with a diamond tip (radius=25nm). The diamond tip was grounded on three sides to yield an apex angle of 60°. The normal load was determined by multiplying the cantilever spring constant by the cantilever deflection. Nanoindentation tests were made in the load range of 12.8–76.5μN with a cantilever stiffness of 255N/m. The indenter tip was used to image and locate an anodized GaAs-oxide structure and then *in-situ* indent it with the same tip. Indents were performed on the anodized structures as a result of a normal load being applied on the surface by the tip. Nanohardness was calculated by dividing the indentation load by the projected residual area.

In Fig.2-9(a) there is a detailed view of the anodized nanowires and nanodots patterns by AFM-based nanoindentation under loads of 12.8–76.5μN. Two lines, one from *A* to *B* and the other from *C* to *D*, pass through a wire and three dots. A cross section of Fig.2-9(a) image is shown in Fig.2-9(b). In Fig.2-9 it can be observed that the indentation depth increases as the normal load is increased. The presence of plastic deformation pile-ups in the vicinity of the indented region, leads to dislocation glide in nanowires more than in nanodots. The nanohardness of the anodized nanowires and the nanodots as a function of indentation depth is shown in Fig.2-9(c). The nanohardness does not manifest any change as the indentation depth is increased

up to ~2nm. The nanohardness of the anodized nanowire at the shallowest indentation depth of 0.6nm is 49.5GPa and it drops to a value of 22.9GPa at an indentation depth of 3.8nm. The nanohardness of the anodized nanodot at the shallowest indentation depth of 0.3nm is 25.9GPa and it drops to a value of 10.8GPa at an indentation depth of 2.3nm.

The data available for mechanical properties of Si, SiO_2, GaAs and AFM tip-induced GaAs oxides are displayed in Table 2-1. As can be noted, AFM tip-induced GaAs oxides exhibit larger hardness values than other semiconductors materials, with the possible deduction that they exhibit the larger internal stress. This is because that large stress is being built up owing to the volume mismatch between the GaAs-oxides and the surrounding non-anodized GaAs during the AFM anodization processes. Of note, the nanohardness of the anodized nanowires is about 2 times higher than the anodized nanodots. From a microscopic view it can be deduced that the cause could be due to the influence by plastic deformation or different geometrical restriction. The nanohardness behavior at indentation depths greater than 2nm can be explained by the plastic deformation occurring from the contact between the structure and the AFM probe tip. The nanohardness drops at indentation depths greater than 2nm this was due to substrate influence and indentation size effect, as mention in Refs.39&40.

2.3 Enhancement of the aspect ratio using CNT probe nanooxidation

Carbon nanotubes (CNTs) are widely used in AFM [41], because the nanotubes are well known to have high aspect ratios (of 10–10^3 provide the ability to probe deep crevices and steep feature), small tip radii of curvature (less than 10nm) and high stiffness. Conventional probe tips are made from Si or Si_3N_4 in the shape of a pyramid or a cone and have a tip radius of curvature of 10nm or often much larger. Nanotubes have considerable mechanical flexibility and can be elastically buckled without damage [41-42]. Therefore, nanotube tips are robust and will not be broken off by an accidental crash on a sample surface, whereas conventional scanning probe tips are easily chipped.

The application of CNT probes for nanooxidation [43] began at almost the same time as the improvement in resolution for image measurement [44]. The high accuracy of positioning and environmental control has yielded profitable results for performing the ultimate precision and high reproducibility in nanofabrication. As a practical requirement, down-sizing of the dense oxide patterns is necessary to develop criterion devices for nanoelectronics, nanooptics and nanomechanics, for instance: increasing the density of recording dots in high-density data storage [45]. Because the size of the fabricated oxide is predominantly determined by the probe apex, it is expected that improvement of the probe will open up great possibilities for miniaturization. An effective way to decrease the probe apex is by using a CNT [46]. Since the diameter of the scanning probe tip determines the imaging resolution, CNT tips would offer high resolution, while the length of CNT tips permits the tracing of rough surfaces with steep and deep features. Herein, in this section, we have investigated the nanooxidation of *p*-GaAs(100) surface using ncAFM with MWCNT

probes which were employed to improve aspect ratios of GaAs-oxides and nanoscale oxide dots, wires and bumps. To adopt the oxide wires and bumps as integral parts of the devices serving as effective tunnel barriers for carrier transport, further improvements of the aspect ratios are needed. By careful control of conditions, the resolution and precision are increased compared to nanofabrication using the standard cantilevers. In addition, we also studied the effect of modulating the voltage in the aspect ratio of the oxide structures grown. Results indicate that the application of an AC voltage to induce the oxidation significantly modifies the aspect ratio of the oxide structures.

§ Experiment details — Using an ambient AFM (Solver-P47, NT-MDT, Russia, 1% accuracy in relative humidity control) the experiments were performed at room temperature with humidity of 55%. A modified cantilever (Daiken-Kagaku, 3N/m, 157kHz) with a conductive multiwalled carbon nanotube (MWCNT, ~10nm in diameter and ~300nm in length) on the Si probe was employed for imaging and nanooxidation, please see Fig.2-10(b). For dots anodization, various 10V pulses, which ranged from 0.02 to 100s, acted on various surface points through AFM tips. For wires anodization, various scan rate which ranged 0.1 to 10μm/s at a constant anodized voltage of 10V. For larger area anodization, AFM tips were scanned backward and forward across a larger area with various sample voltages that ranged from 6 to 10V, and the scan rates were 5, 10 and 15μm/s.

A square waveform pulsed voltage was applied to the CNT tip of AFM in the nanooxidation process. Five parameters, namely the high level (V_{ox}) and low level (V_{res}) of the voltage amplitude, their corresponding durations (T_{ox} and T_{res}) and the number of voltage pulses (N) applied on each scanning point, please see Fig.2-14(a), which determining the actual voltage mode applied to the tip. The value of these

parameters can be adjusted separately. In the present works, V_{res} was set to zero at all times. When T_{res} was set to zero, a static voltage was actually applied to the tip. Changing the values of T_{res} and T_{ox} could apply desired voltage pulses to the tip. A series of oxide structures were fabricated by tip-induced local oxidation with various exposure conditions.

§ Fabrication of the dots, wires and bumps by AFM nanooxidation with CNT tip

The nanooxidation proceeds through a water meniscus between the tip and the sample while applying an anodized voltage, as shown in Fig.2-10. Fig.2-11(a) shows an AFM image in which a series of point oxide protrusions, from right to left, are produced via 10V pulses of 5, 10, 30, 60 and 100s, respectively. Observably, the average full width at half maximum of the point oxide protrusions is ~200nm, and the protruded point oxide height increases concurrently with pulse time, please see the height profile of Fig.2-11(a). This indicates that oxide growth follows the direction (perpendicular to the surface) of the electric field with time. Notably, this experimental result is similar to those presented previously [4] regarding anodization at varying static voltages and pulse for the duration. Kinetic measurements are shown in Fig.2-11(b) where the height of the oxide dots under the CNT and/ the conductive tip apex is plotted as a function of the anodization time. From Fig.2-11(b)&(c), it is clear that the oxide dots height and the aspect ratio of *p*-GaAs(100) oxide dots could be improved using the CNT tip.

As mentioned in the above section §2.1-2, the bias dependence of the rate indicates that the electric field plays an important role in the oxidation process. Very high initial growth rates were observed (for both CNT and conductive tips) at extreme electric field strength near the tip apex of up to ~10^8V/cm. It can be seen from Fig.2-11(d) that the growth rate of oxidation is not only a function of electric field

strength, but also appears to depend on the applied bias voltage. This also indicates that the observed kinetics does not obey the simple Cabrera-Mott model [22] because of the mechanical stress built up between GaAs and $Ga(As)O_x$ during oxidation mainly. The details have been discussed in section §2.1-2.

To investigate the dependence of the oxide wire pattern on the scanning rate of the CNT and/ conductive tip, the scanning rate was varied between 0.1 and 10μm/s at an anodized voltage of -10V. These results are shown in Fig.2-12. The wires shown in Fig.2-12(a) were formed by scanning the CNT tip with scanning rates of 0.1, 1 and 10μm/s, respectively. With an increase in scanning rate from 0.1 to 10μm/s, the width and the height of the anodized wire were significantly decreased (for both CNT and conductive tips) as shown in Fig.2-12(b). In terms of the oxidation of silicon, it has been reported that the height of the oxidized area varies with increasing scanning rates (υ) of the tip and is proportional to log(1/υ) [4], $\upsilon^{-1/2}$ [47] and $\upsilon^{-1/4}$ [25] for a given bias. Nevertheless, a quantitative model has not yet been proposed to explain these observations. In this work, the height of the GaAs oxide pattern was found to be proportional to log(1/υ) at a tip bias voltage of -10V as illustrated by fitting the dotted line in Fig.2-12(b).

To more thoroughly understand the anodic oxidation, the larger area (bumps) oxidation by using a moving tip is presented. In Fig.2-13(a), an AFM image reveals that there is an array of 9 rectangular oxide bumps on *p*-GaAs(100) surface. The average size of the oxide bump is ~400×500nm^2. Fig.2-13(a) illustrates three rows of the oxide bumps, from top to down where are obtained at the sample voltages (6, 8 and 10V). And, various scan rates, 5, 10 and 15μm/s, respectively, are used. It can be confirmed from Fig.2-13(a), the heights of the three oxide bumps are proportional to the sample voltages but independent of the scan rates. This experimental results agree with the reported previously studies [25-26]. Fig.2-13(b) demonstrates a graph, which

compares height to sample voltage for CNT and conductive tips. It indicates that the height of the oxide bumps is linearly dependent on the anodized voltage for both cases. In addition, it is found that the anodized oxides on the surface became rougher at faster scanning rate.

Comparing the experimental height results of the oxide dot (Fig.2-11(a)) and bump (Fig.2-13(a)) at the anodized voltage of 10V, the height of the former is ~9nm and smaller than that of the latter which is ~10nm. An oxide structure was obtained by applying a bias voltage to an AFM probe that was at a fixed point on the surface. As an AFM tip begins to scan the surface forward from the initial point, a series of oxide dots appears at sequential static voltage pulse. Thus, the latter oxide dots are higher than the former ones because of the latter oxide dots which grow constantly at a range of the neighboring voltage pulses, until the voltage pulse power is terminated. When the tip sweeps back and forth, the growth process repeatedly forms an oxide bump.

§ Voltage modulation studies by AFM nanooxidation with CNT tip

The use of an AFM as an active tool to realize GaAs nanolithography is presented in §2.1-1, using a continuous voltage applied between the AFM tip and the surface. The main drawback of this technique is the poor reliability of the tip due to the strong tip-surface interaction. An original way which both increases the reliability and improves the nanolithography resolution is the use of pulsed voltages instead of continuous polarization.

Additional control of the oxidation process can be obtained if the anodized voltage is modulated. The dimensions of the oxide structures change if an AC voltage is applied instead of a DC voltage; please see Fig.2-14(b). The parameters that define the AC waveform are illustrated in Fig.2-14(a), in which the waveform consists of a

series of pulses where T_{ox}, V_{ox} and T_{res} are denoted as the oxidation time, the applied voltage and the rest time, respectively. It has been verified that the application of a DC voltage at V_{res} cannot produce any appreciable oxidation on the surface. The total oxidation time is T_{ox} multiplied by the number of pulses. We refer to $1/(T_{ox}+T_{res})$ as the frequency of the waveform. In Figs.2-14(b)&(c), two oxide dots were grown by applying AC and DC, right and left, respectively. It was observed that AC and DC produce a similar width at the base of the dot. Nevertheless, the dot formed under AC conditions presents a height increase, at the central part of the dot where the electric field is supposed to be higher. Under these conditions, the increase of height and aspect ratio is around 1.1. This result has also been obtained by Dagata *et al*. [5].

In the case of a pulse voltage applied, the continuous transport of the OH^- ions will be broken in the rest duration (T_{res}) of the voltage pulse and the oxidation process will be stopped. When the next voltage pulse is active, the directional transport of the OH^- ions should be reinitialized because the OH^- ions go randomly in the rest period of the last voltage pulse. As a result, the oxidation process cannot continue from where it stopped but must restart from the beginning. This process repeated within the applied voltage pulses and caused the reduction of the lateral growth rate of oxide. If the active duration of the pulse (T_{ox}) is sufficient shot and the initial stage of the lateral growth is disturbed, a strong suppression of the oxide growth in which could be achieved.

As mentioned above, the height enhancement under modulation voltage conditions (Fig.2-14) can be related to the space charge build-up within the oxides. The oxidation reaction is a source of hydrogenous species. The proton concentration increases after long pulse time, with $H^+ + OH^- \rightarrow H_2O$ neutralization reaction becoming significantly, please refer to the details of §2.1-1. As less OH^- ions arrive

at the GaAs/Ga(As)O_x interface, this in turn, implying a decrease of the oxidation rate, please see Fig.2-11(d). According to the present experiments, this effect can be reduced by means of the applied AC voltage pulses. The negative part of the voltage pulse decreases the concentration of H^+ in the oxide structures. Thus, the oxidation rate is higher at the conditions of AC voltage pulses; *i.e*. a pulsed voltage enables us to fabricate significantly improved high aspect ratio oxide structures compared to the conventional AFM anodization process by using continuous bias.

2.4 Electrical properties of AFM tip-induced GaAs oxides

Local oxidation using an AFM is a promising scanning-probe-based lithographic technique suitable for fabrication of nanoscale structures and devices. There are two possibilities for using the electric field-induced nanooxidation method for nanoscale device fabrication; one is as a mask for lithography and the other is as an insulator for field isolation, interlayer dielectric film, or gate oxide of a metal-oxide-semiconductor (MOS) structure. As for the previous usage, it has been reported that a field-induced nanooxidation surface is usable as a robust mask for wet etching and dry etching [6]. Nevertheless, as for the latter usage, there have been relatively few attempts, probably because the electrical properties of the AFM field-induced nanooxidation surface have not been sufficiently investigated yet.

The understanding of the AFM field-induced nanooxidation surface properties,

especially its *I-V* characteristics, is a major issue for the usage as insulator films of nanoscale devices. Herein, in this section, *I-V* characteristics of the field-induced nanooxidation surface are studied.

§ Experiment details — To study the electrical characterizations of the GaAs oxide nanodots, the *I-V* measurements were done at room temperature. *I-V* characteristics were measured with an AFM system and were compared before and after the fabrication of GaAs oxide nanodot by using the same conductive tip as that used for the tip-induced oxidation. GaAs oxide nanodots were fabricated by applying an anodized voltage of 10V for 10s in a relative humidity of 60%.

Fig.2-15(a) shows two measured *I-V* curves that correspond to the anodized area and to the non-anodized area. The two curves are obviously different due to the difference in oxide thickness. In the simplest case, the *Fowler-Nordheim* (*FN*) tunneling [48] has been investigated in MOS structures where it has been shown to be the dominant current mechanism. The calculation of current was based on the Wentzel-Kramers-Brillouin (WKB) approximation yielding the following relationship between the current density (J_{FN}) and the electric field in the oxide (E_{oxide}):

$$J_{FN} = C_{FN}\, E_{oxide}^{2} \exp\left(-\frac{\beta}{E_{oxide}}\right) \tag{6}$$

where C_{FN} and β are given by

$$C_{FN} = \frac{q^3}{16\pi^2 \hbar \phi_B} \quad \text{and} \quad \beta = \frac{4}{3}\frac{\sqrt{2m_e^* \phi_B^3}}{\hbar q} \tag{7}$$

where the $\hbar$ is Plank's constant, q is the magnitude of charge of an electron, ϕ_B is the barrier height and, m_e^* is the effective electron mass in the oxide. In order to check

for this current mechanism, the *I-V* characteristics was plotted as a FN plot $\ln(J_{FN} / E_{oxide}^2)$ vs. $1/E_{oxide}$, this equation is displayed by a straight line whose slope (β) determines the barrier height (ϕ_B). The energy band diagram for the metal tip/*p*-GaAs(100) oxides/*p*-GaAs(100) heterostructure in the $V > 0$ bias range can be illustrated in Fig.2-15(b). Note that the current before the AFM nanooxidation did not follow the FN tunneling model because of the native oxide on the GaAs substrate surface, in which the mechanism of current across such oxide layer could be explained by a direct tunneling of electrons [49].

Fig.2-16(a) shows the *I-V* curve of the anodized region from the first quadrant of Fig.2-15(a). The modified FN plot of $\ln\left(I/V^2\right)$ vs. $1/V$ of the *I-V* curve is displayed in Fig.2-16(b). Here it was assumed that (i) the applied bias voltage drops across the GaAs oxides and, (ii) GaAs oxide thickness is given by $t_{oxide} \approx 1.5h_{oxide}$ [23], where h_{oxide} is the oxide height measured by AFM. Here t_{oxide}=8.7nm and the diameter of the GaAs oxide nanodot is ~150nm. It can be seen from Fig.2-16(b) that FN plot follows a linear relationship within the bias range and, thus the electron transport across the GaAs oxide nanodot of a given thickness, from the metal tip into the GaAs substrate, is because of the FN tunneling mechanism. The slope of the FN plot displayed in Fig.2-16(b) should then give $-\beta t_{oxide}$. However, ϕ_B is sensitive to the presence of a water layer and thus the exact value could not be obtained from this work.

2.5 Conclusions

The electrochemical oxidation characteristics of *p*-GaAs(100) surface by ncAFM were investigated. The application of a bias voltage between a conductive tip /and a CNT tip separated a few nanometers from a *p*-GaAs(100) surface allows the field-induced formation of nanometer-size water menisci that can subsequently be used to fabricate nanometer-size oxide structures. Their sizes were dependent on the relative humidity, the scanning rate of the tip and the anodization time.

Once the voltage was applied to the tip, the OH^- ions drifted to the sample surface under the produced electric field, but their drifting speeds were different spatially and the ions would arrive at the surface at the different time. With increasing the anodization time, the growth rate of oxides rapidly decreased. The anodic oxidation process is enhanced when the electric field strength is of the order of $2–3\times10^7$V/cm. This result can be attributed to the decrease of the transport rate of ionic species through the existing oxide layer because of a reduction of electric field strength with increasing the oxide thickness, indicating that the growth of nanodots is limited by the field-enhanced diffusion mechanisms of OH^- ions through the oxides. At a relative humidity of 70% a “two-storied” shaped nanodot caused by the ionic diffusion was found. Evidence of oxides growth on GaAs surface due to AFM tip-induced oxidation was confirmed by AES analysis. Nanohardness of the anodized nanowires and nanodots is the range of 22.9–49.5GPa and 10.8–25.9GPa, respectively. Results carried out on sample of anodized nanowires and nanodots exhibit that an ISE on the mechanical properties becomes significantly at a threshold point as the indentation depth is of 2nm. In addition, the *I-V* characteristics of the electric field-induced oxidation GaAs surface shows a FN tunneling current model.

On the other hand, CNT-attached AFM probes are successfully used to fabricate

the nanometer oxide dots, wires and bumps. This study revealed that the pulsed bias has an advantage for obtaining a higher aspect ratio pattern than the continuous bias by reducing the effect of space charge in oxides. This technique trends to increase the tip reliability as to the lithography resolution. Fabrication of nanometer-scale high aspect ratio patterns for various nanodevices is expected by applying our method at the optimized conditions.

References

[1] J.A. Dagata, J. Schneir, H.H. Harary, C.J. Evans, M.T. Postek and J. Bennett, Appl. Phys. Lett. 56 (1990) 2001.
[2] H. Sugimura and N. Nakagiri, Jpn. J. Appl. Phys. 34 (1995) 3406.
[3] Y.F. Lu, Z.H. Mai, G. Qiu and W.K. Chim, Appl. Phys. Lett. 75 (1999) 2359.
[4] P. Avouris, T. Hertel and R. Martel, Appl. Phys. Lett. 71 (1997) 285.
[5] J.A. Dagata, T. Inoue, J. Itoh and H. Yokoyama, Appl. Phys. Lett. 73 (1998) 271.
[6] F.S.S. Chien, J.W. Chang, S.W. Lin, Y.C. Chou, T.T. Chen, S. Gwo, T.S. Chao and W.F. Hsieh, Appl. Phys. Lett. 76 (2000) 360.
[7] K. Unal, B.O. Aronsson, Y. Mugnier and P. Descouts, Surf. Interface Anal. 34 (2002) 490.
[8] N. Farkas, G. Zhang, E.A. Evans, R.D. Ramsier and J.A. Dagata, J. Vac. Sci. Technol. A 21 (2003) 1188.
[9] K. Watanabe, Y. Takemura, Y. Shimazu and J. Shirakashi, Nanotechnology 15 (2004) S566.
[10] E.S. Snow and P.M. Campbell, Appl. Phys. Lett. 64 (1994) 1932.
[11] J. Shirakashi, K. Matsumoto, N. Miura and M. Konagai, Appl. Phys. Lett. 72 (1998) 1893.
[12] H.C. Day and D.R. Allee, Appl. Phys. Lett. 62 (1993) 2691.
[13] B. Irmer, M. Kehrle, H. Lorenz and J.P. Kotthaus, Appl. Phys. Lett. 71 (1997) 1733.
[14] R. García, M. Calleja and F. Pérez-Murano, Appl. Phys. Lett. 72 (1998) 2295.
[15] M. Tello and R. García, Appl. Phys. Lett. 79 (2001) 424.
[16] R. García and A.S. Paulo, Phys. Rev. B 60 (1999) 4961.
[17] R. García and A.S. Paulo, Phys. Rev. B 61 (2000) R13381.

[18] A.S. Paulo and R. García, Phys. Rev. B 66 (2002) 041406.
[19] S. Gómez-Moñivas, J.J. Sáenz, M. Calleja and R. García, Phys. Rev. Lett. 91 (2003) 056101.
[20] M. Calleja, M. Tello and R. García, J. Appl. Phys. 92 (2002) 5539.
[21] S.K. Ghandhi, *VLSI Fabrication Principle* (Wiley, New York, 1994).
[22] N. Cabrera and N.F. Mott, Rep. Prog. Phys. 12 (1949) 163.
[23] Y. Okada, S. Amano, M. Kawabe, J.S. Harris and Jr., J. Appl. Phys. 83 (1998) 7998.
[24] J. A. Dagata, T. Inoue, J. Itoh, K. Matsumoto and H. Yokoyama, J. Appl. Phys. 84 (1998) 6891.
[25] T. Teuschler, K. Mahr, S. Miyazaki, M. Hundhausen and L. Ley, Appl. Phys. Lett. 67 (1995) 3144.
[26] D. Stiévenard, P.A. Fontaine and E.Dubois, Appl. Phys. Lett. 70 (1997) 3272.
[27] H. Sugimura, T. Yamamoto, N. Nakagiri, M. Miyashita and T. Onuki, Appl. Phys. Lett. 65 (1994) 1569.
[28] H. Sugimura, T. Uchida, N. Kitamura and H. Masuhara, Appl. Phys. Lett. 63 (1993) 1288.
[29] H. Kuramochi, K. Ando, and H. Yokoyama, Surf. Sci. 542 (2003) 56.
[30] H. Jungblut, D. Wille, and H.J. Lewerenz, Appl. Phys. Lett. 78 (2001) 168.
[31] H. Sugimura, T. Uchida, N. Kitamura and H. Masuhara, J. Phys. Chem. 98 (1994) 4352.
[32] H. Kuramochi, K. Ando and H. Yokoyama, Jpn. J. Appl. Phys. 42 (2003) 5892.
[33] Lide, David R. ed., *CRC Handbook of Chemistry and Physics* (CRC, Boca Ration, FL, 1994).
[34] J.I. Shirakashi, K. Matsumoto and M. Konagai, Appl. Phys. A 66 (1998) S1083.
[35] Y. Okada, Y. Iuchi, M. Kawabe, J.S. Harris and Jr., J. Appl. Phys. 88 (1998) 1136.
[36] G.M. Pharr, W.C. Oliver, R.F. Cook, P.D. Kichner, M.C. Kroll, T.R. Dinger and D.R. Clarke, J. Mater. Res. 7 (1992) 961.
[37] J.B. Pethica, R. Hutchings and W.C. Oliver, Phil. Mag. A 48 (1983) 593.
[38] E.P. Trifonanva and L. Hitova, Thin Solid Films 224 (1993) 153.
[39] B. Bhushan and X. Li, Int. Mater. Rev. 48 (2003) 125.
[40] W.D. Nix and H. Gao, J. Mech. Phys. Solids 46 (1998) 411.
[41] H. Dai, J.H. Hafner, A.G. Rinzler, D.T. Colber and R.E. Smalley, Nature 384 (1996) 147.
[42] E.W. Wong, P.E. Sheehan and C.M. Lieber, Science 277 (1997) 1971.
[43] H.J. Dai, N. Franklin and J. Han, Appl. Phys. Lett. 73 (1998) 1508.
[44] A. Okazaki, T. Kishida, S. Akita, H. Nishijima and Y. Nakayama, Jap. J. Appl. Phys. 39 (2000) 7067.
[45] E.B. Cooper, S.R. Manalis, H. Fang, H. Dai, K. Matsumoto, S.C. Minne, T, Hunt and C.F. Quate, Appl. Phys. Lett. 75 (1999) 3566.
[46] S. Iijima, Nature 354 (1991) 56.
[47] M. Yasutake, Y. Ejiri and T. Hattori, Jpn. J. Appl. Phys. 32 (1993) L1021.
[48] M. Lenzlinger and E.H. Snow, J. Appl. Phys. 40 (1969) 278.
[49] T. Kato, M. Matsuda and T. Hattori, Jpn. J. Appl. Phys. 34 (1995) L609.

Table 2-1. Values of the hardness obtained in this present work compared with previously reported for the semiconductors studied.

Materials	Hardness (GPa)
Si(110)	12 [36]
SiO_2	8.3 [37]
GaAs(001)	6.7~7 [38]
p-GaAs(100)	9.5~10.8 [*]
Tip-induced *p*-GaAs(100) oxide	Dot: 10.8~25.9 [*] Wire: 22.9~49.5 [*]

[*]: this present work

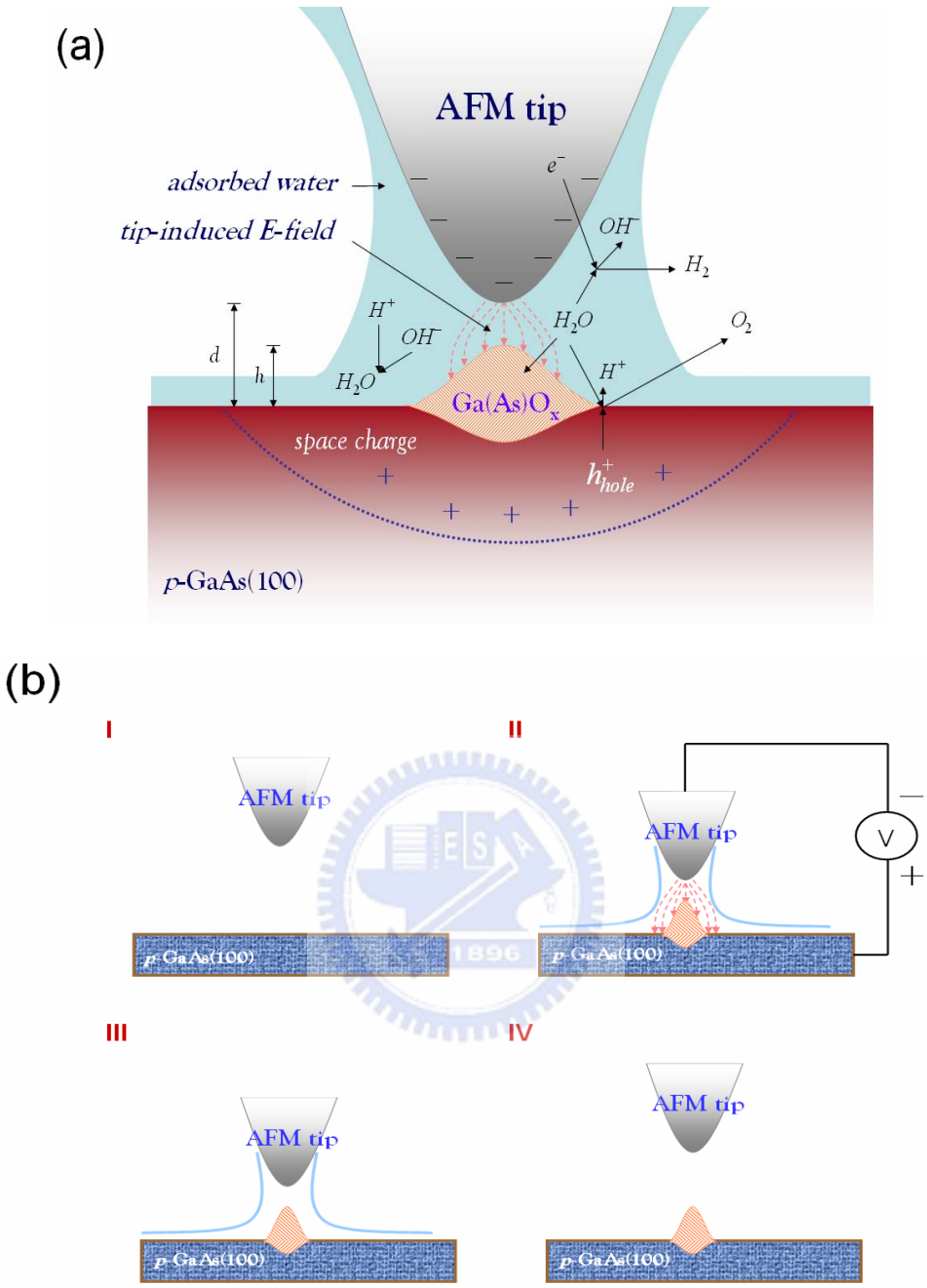

Figure 2-1. (a) Schematic of the principle of AFM anodization. Here, d, h and d-h are the tip-sample distance, the height of grown oxide and the separation between the top of the oxide dot and the AFM tip, respectively; (b) An AFM tip is placed above the sample surface (I) and, then a voltage is applied. The voltage deflects the cantilever, reduces the oscillation amplitude, and drives the formation of water menisci (II). The nanooxidation process starts and a nanometer-size feature is created. After the voltage pulse is off, the attractive force of water menisci reduces the tip oscillation (III). Finally, an AFM tip as retracted and original oscillation amplitude is recovered (IV).

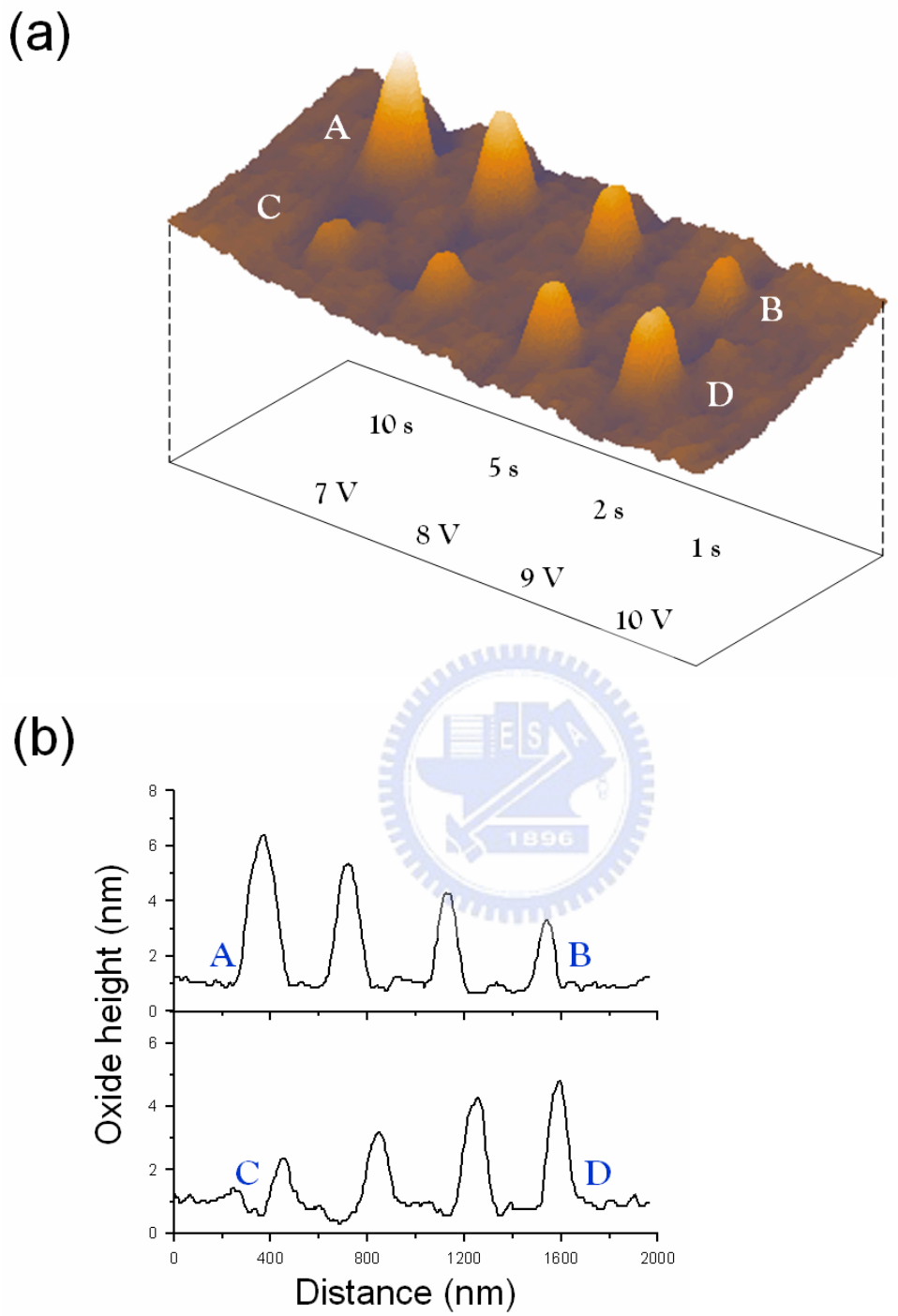

Figure 2-2. (a) An AFM image of nanodots on a p-GaAs(100) surface (1×2μm²); (b) The height profiles of the row 1 and row 2.

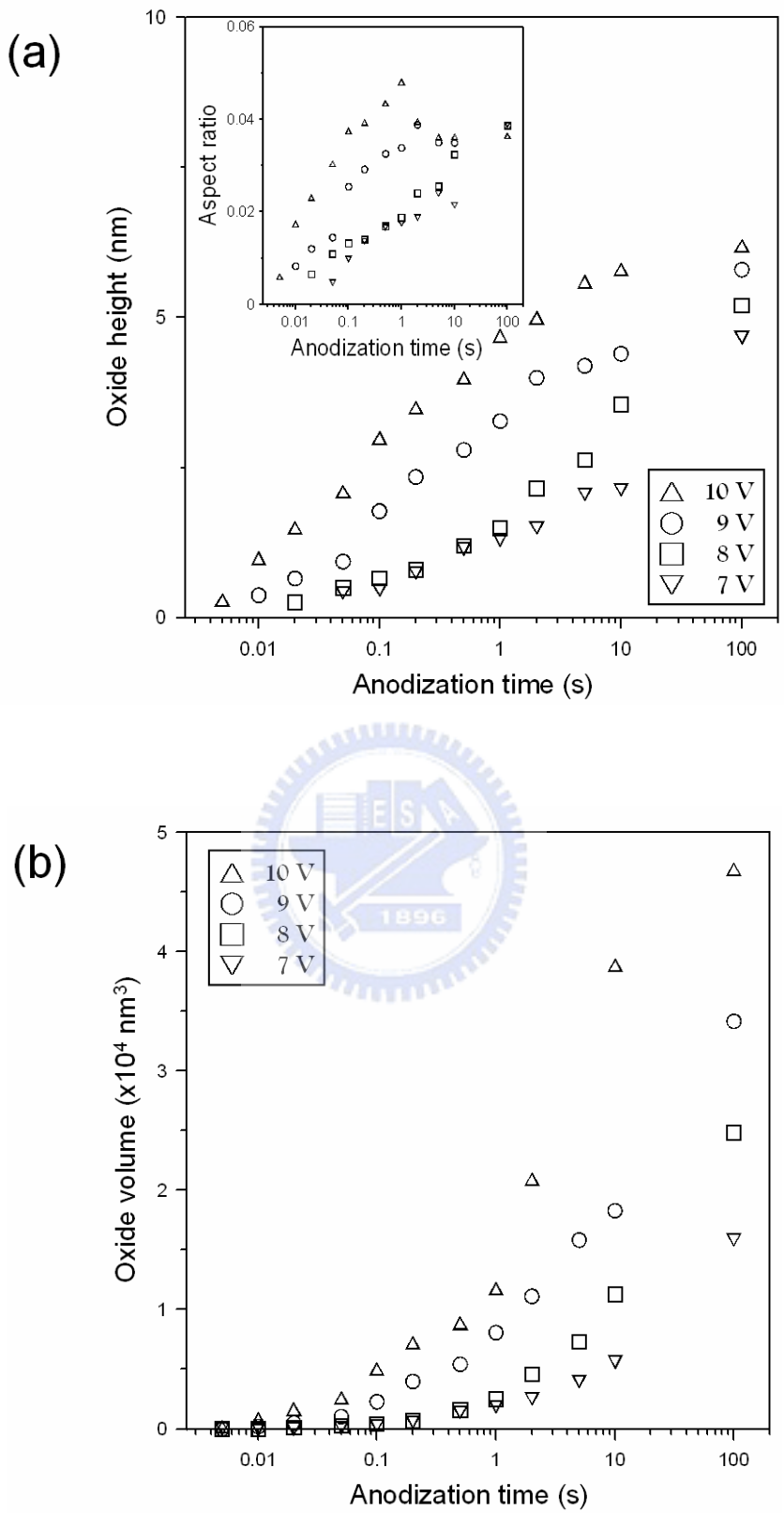

Figure 2-3. (a) Oxide height and the aspect ratio as a function of the anodization times on different anodization voltages; (b) Volume of the oxidized dots as a function of the anodization times at a relative humidity of 70%.

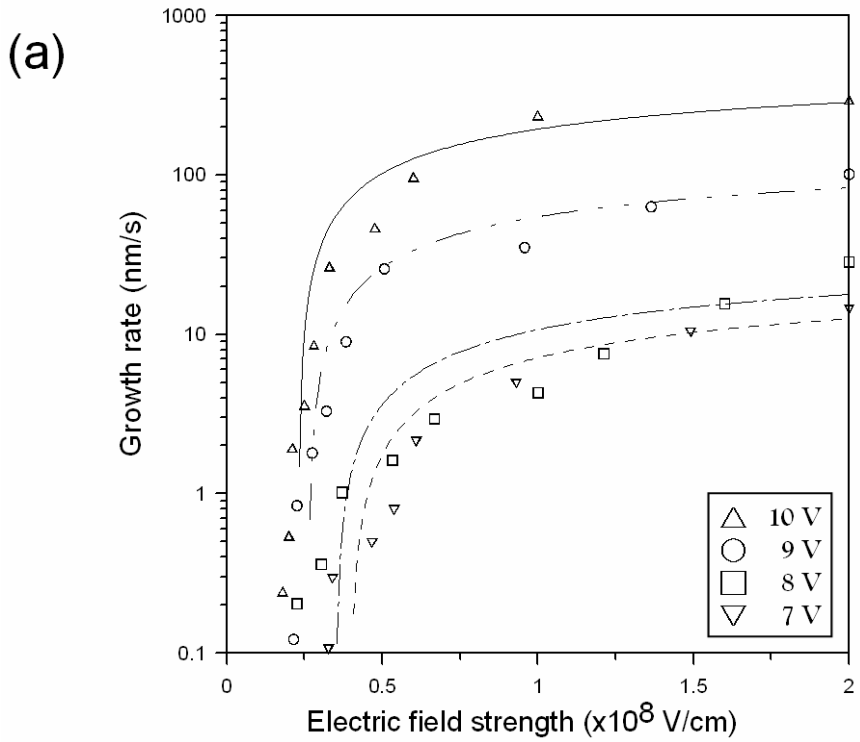

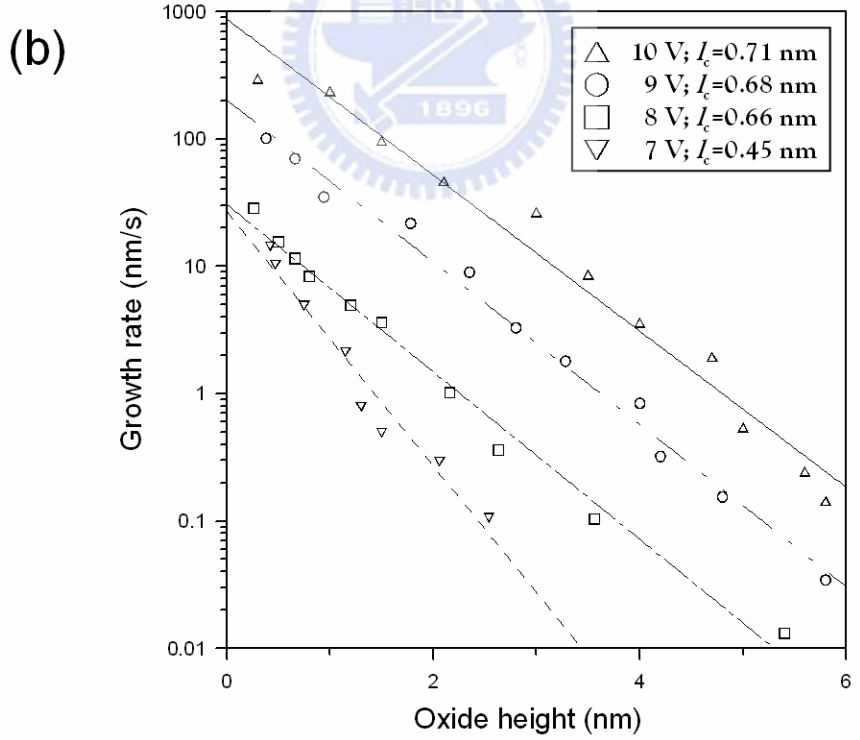

Figure 2-4. (a) Relationships of the growth rate and the electric field strength; (b) Relationships of the growth rate and the oxide height.

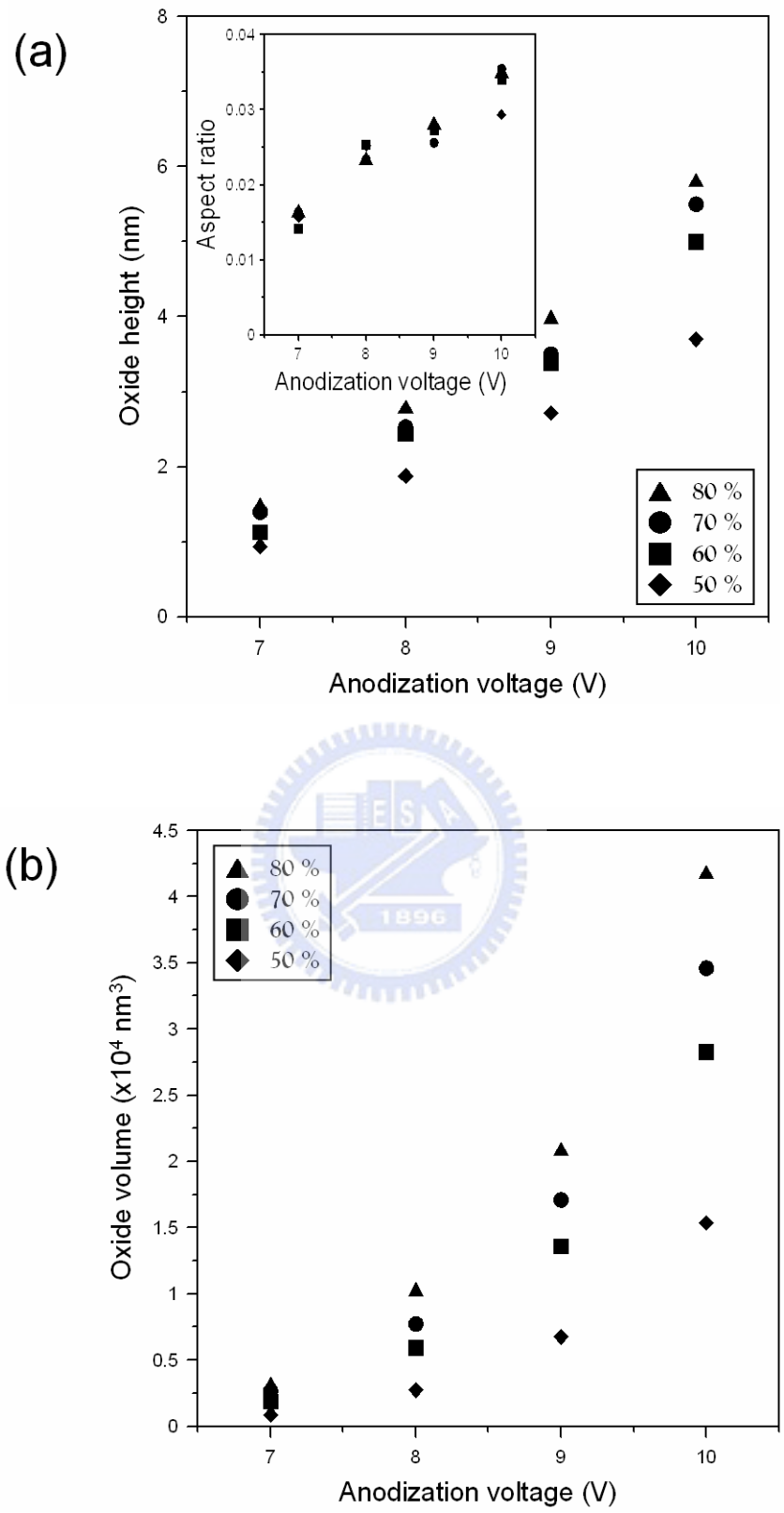

Figure 2-5. (a) Oxide height and the aspect ratio as a function of the anodization voltages on different relative humidity; (b) Volume of the oxidized dots as a function of the anodization voltages at anodization time of 10s.

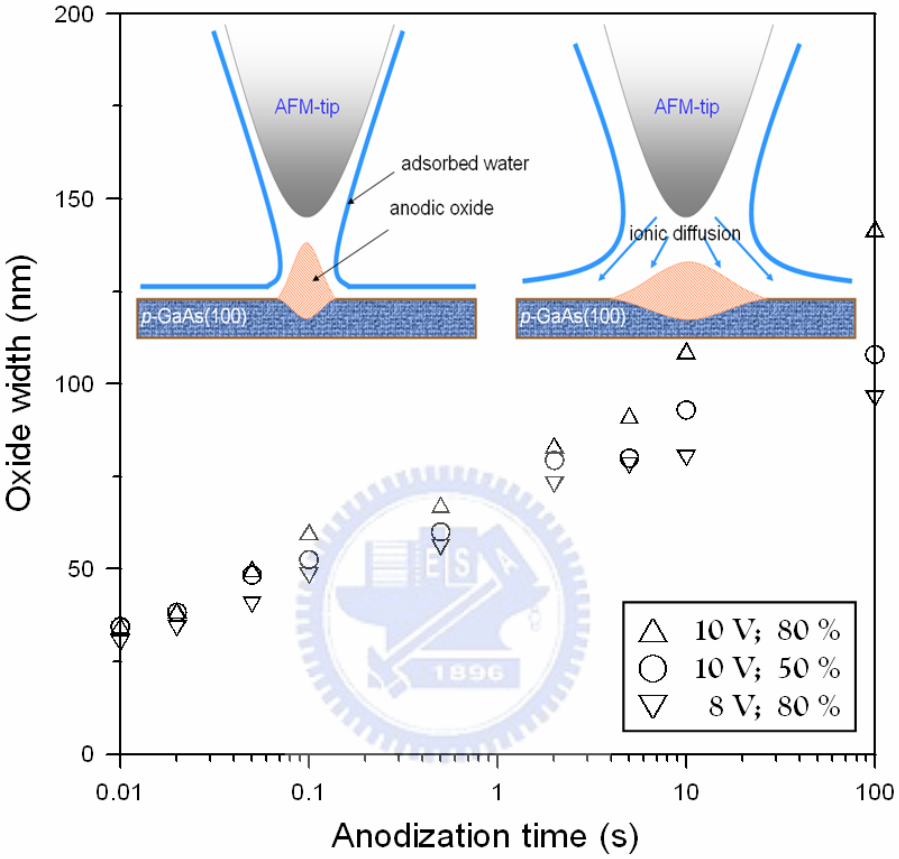

Figure 2-6. Relationships of the oxide width and the anodization time. The insert illustrates the low and high humidity conditions.

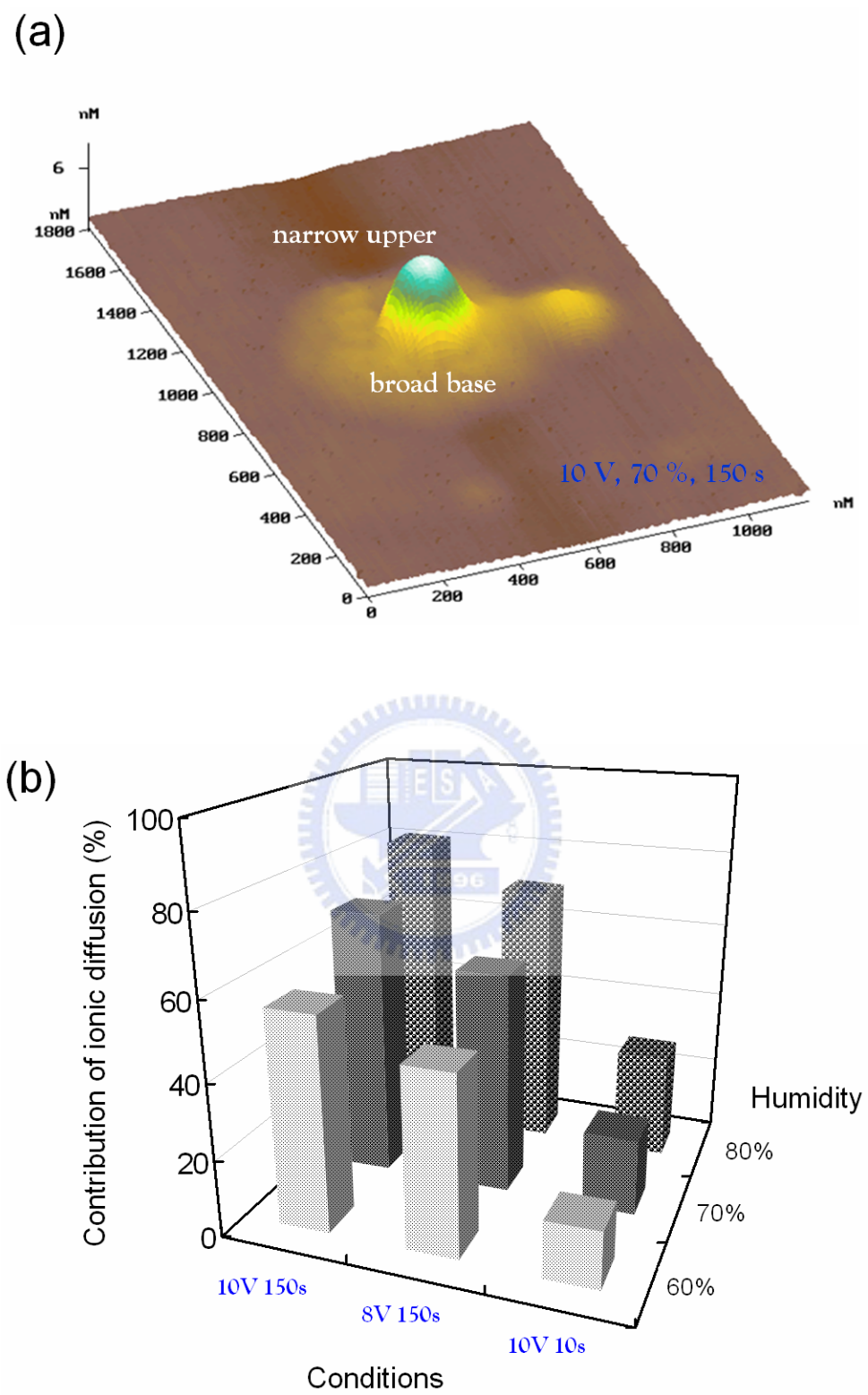

Figure 2-7. (a) A "two-storied" anodized shape dot with the broad base and the narrow upper parts; (b) The contribution of ionic diffusion to anodized dots.

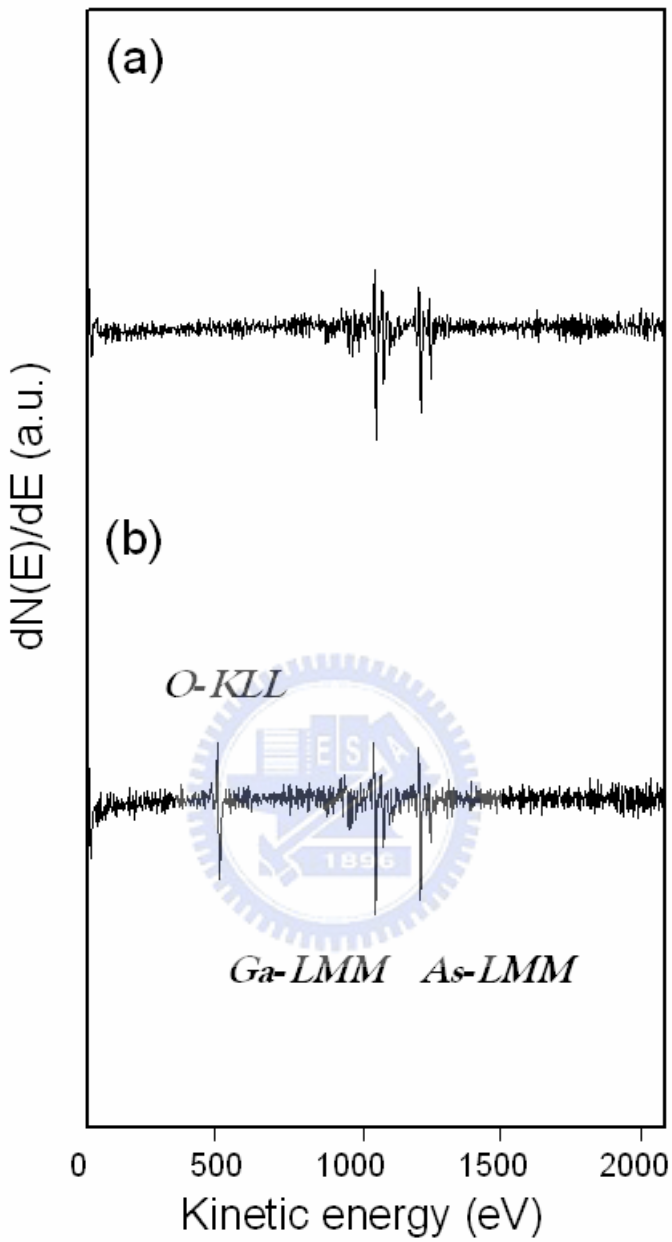

Figure 2-8. AES spectra of (a) the as-grown and (b) the anodized oxide areas on p-GaAs(100) surface.

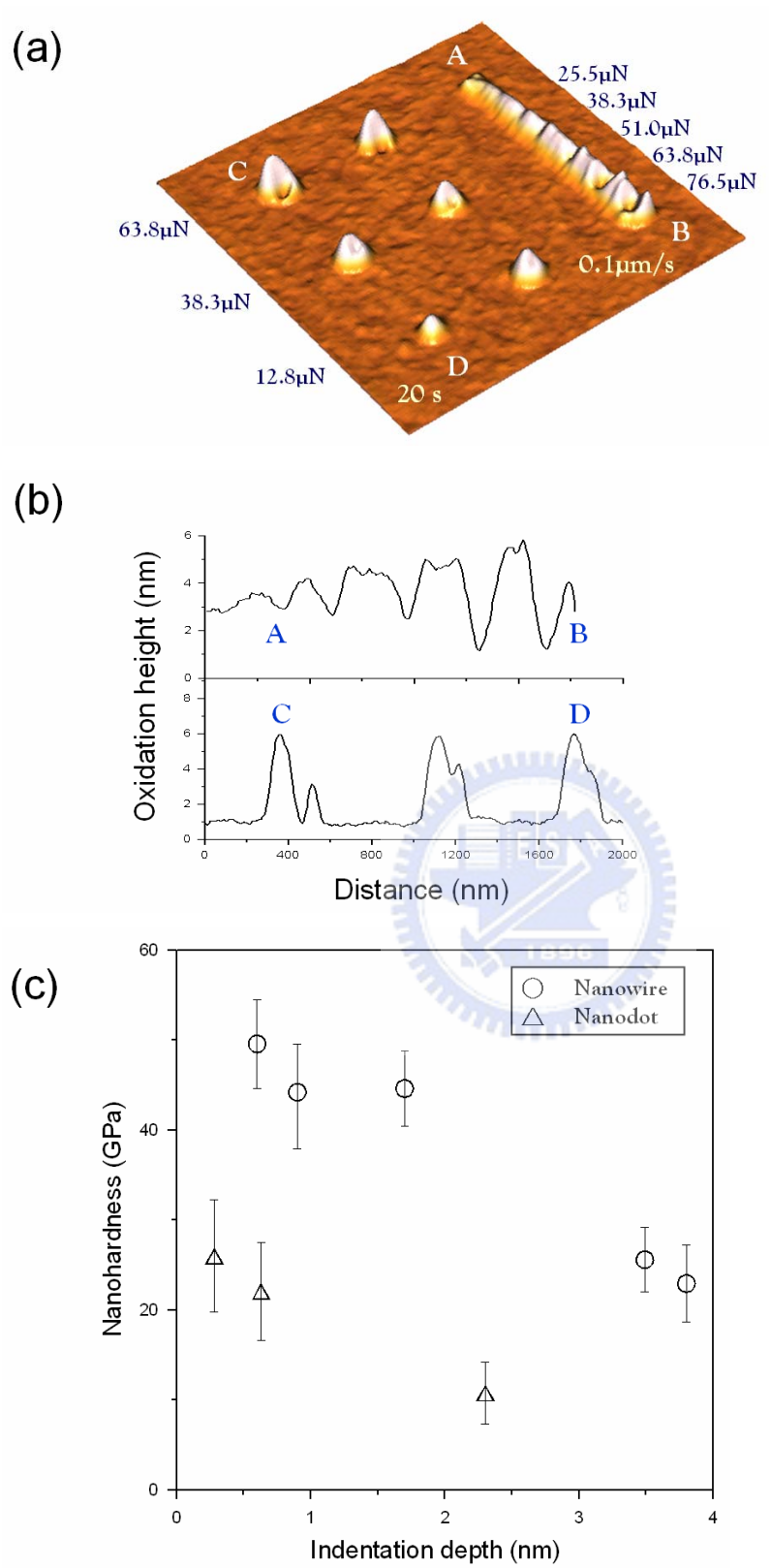

Figure 2-9. (a) An AFM image of the anodized nanowires and nanodots under different loads at an anodized voltage of 10V at relative humidity of 70%. (2.5×2.5μm²); (b) A cross section of the anodized nanowires and nanodots; (c) Nanohardness as a function of indentation depth for the anodized structures.

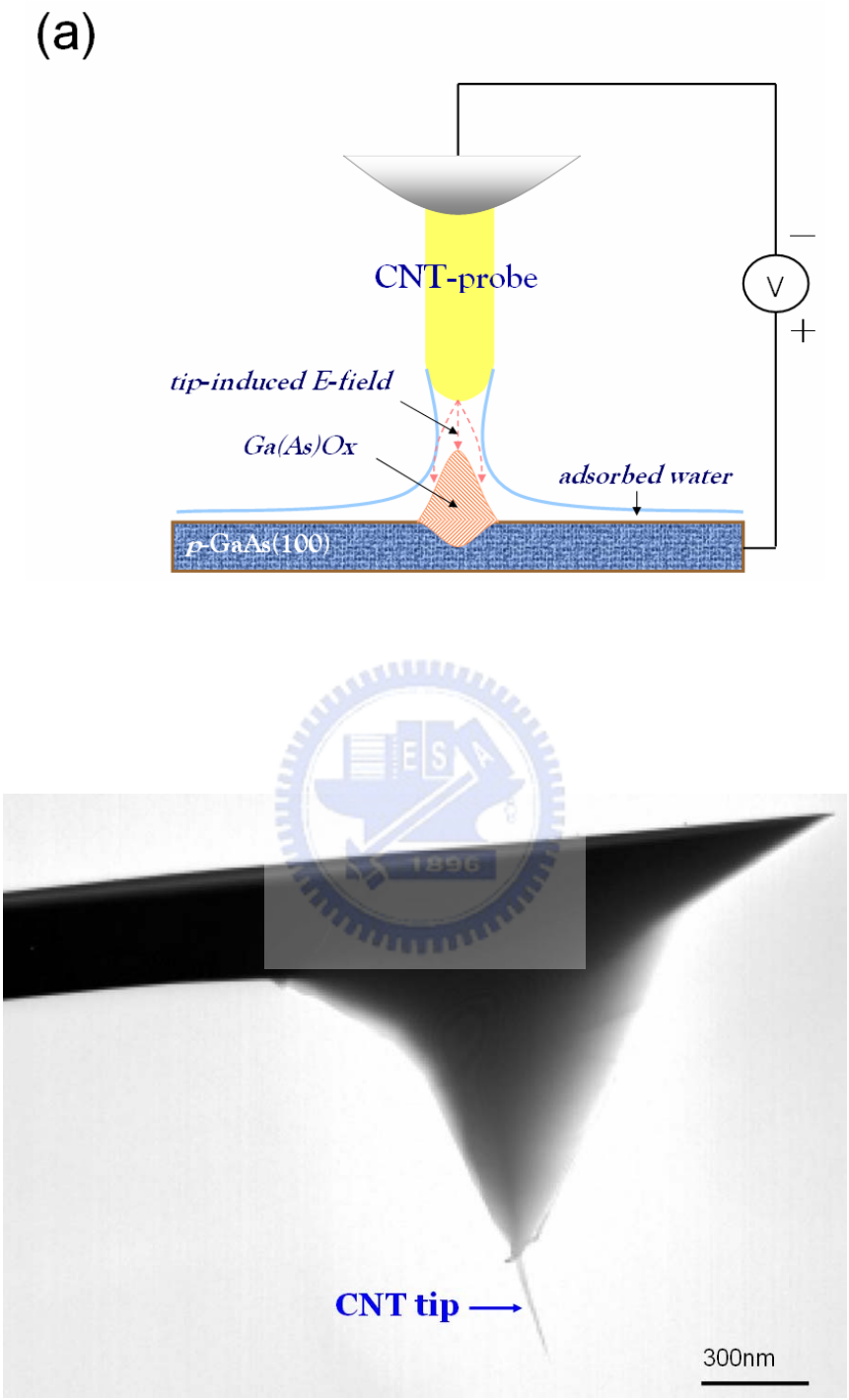

Figure 2-10. (a) Schematic drawing of nanooxidation using a CNT probe tip; (b) SEM image of a CNT fixed onto a conventional Si tip for AFM.

(a)

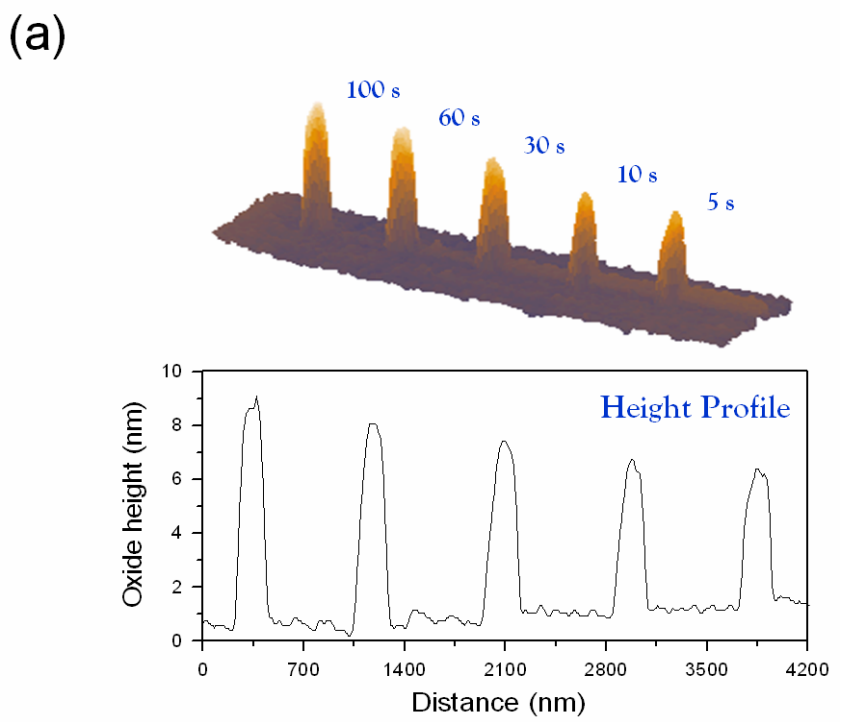
100 s
60 s
30 s
10 s
5 s
Height Profile
Oxide height (nm)
Distance (nm)
0
2
4
6
8
10
0
700
1400
2100
2800
3500
4200

(b)

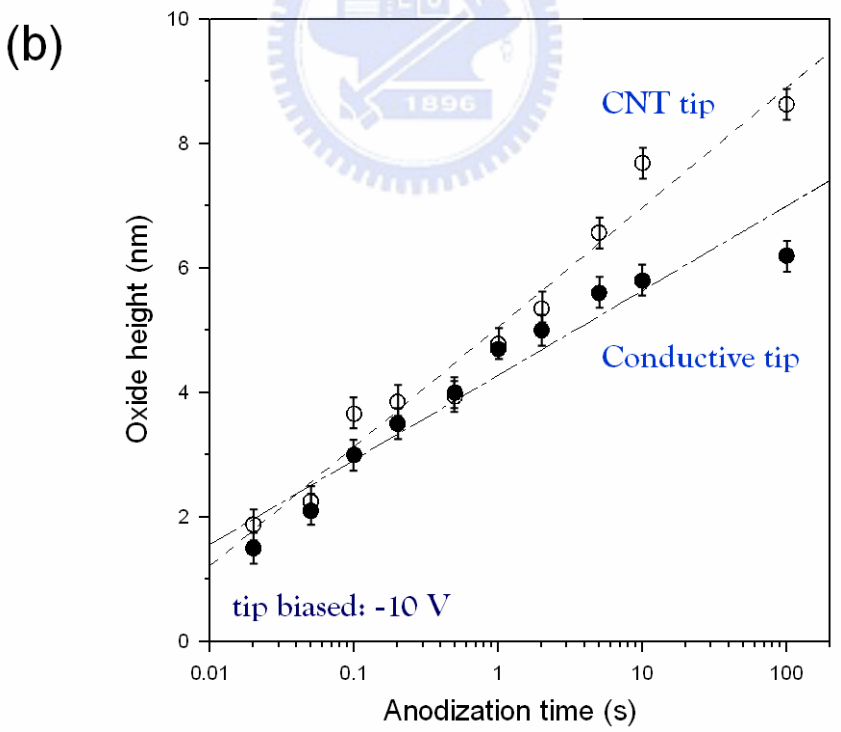
CNT tip
Conductive tip
tip biased: -10 V
Oxide height (nm)
Anodization time (s)
0
2
4
6
8
10
0.01
0.1
1
10
100

(Continue)

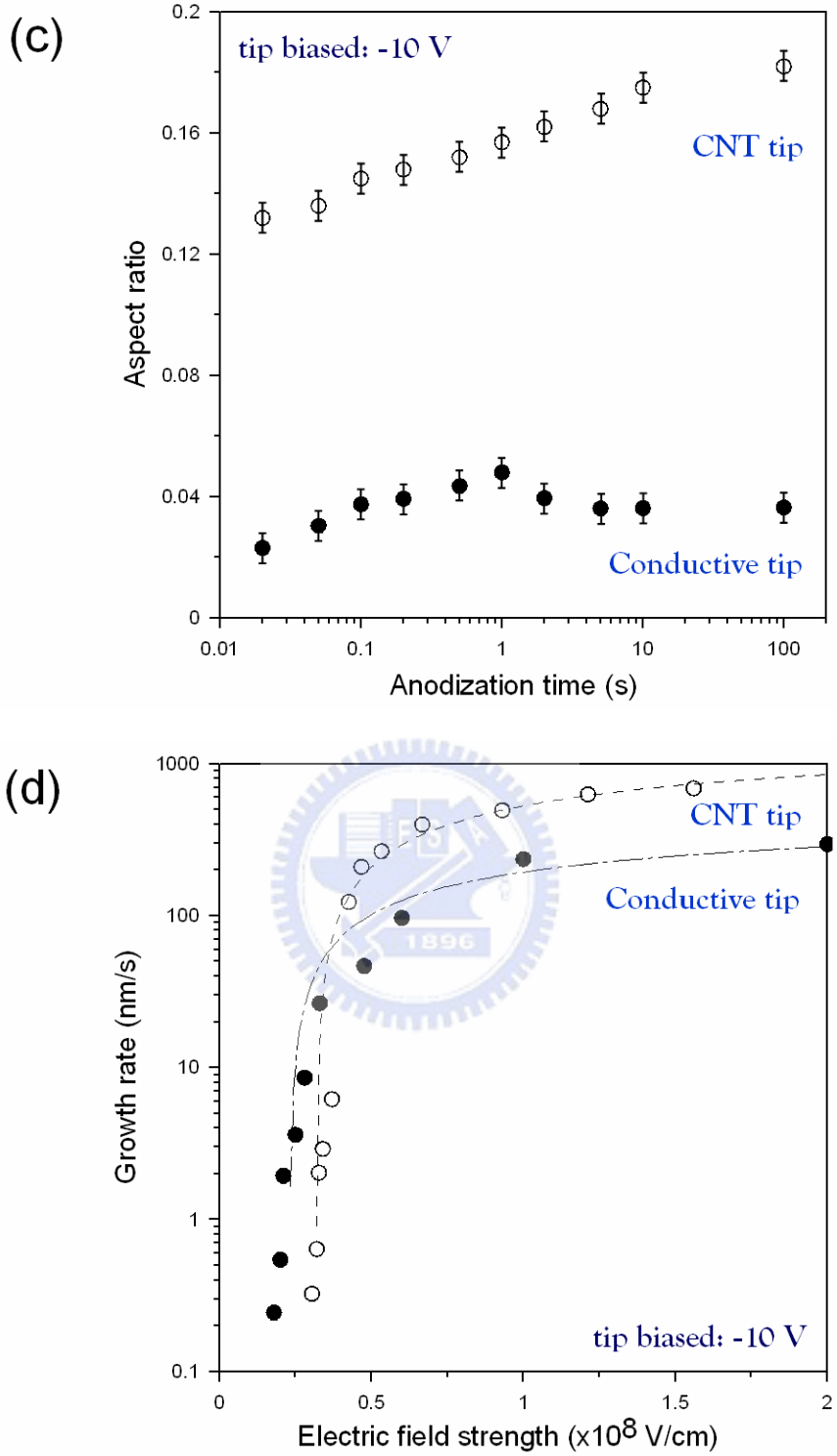

Figure 2-11. (a) An AFM image displaying a series of point oxide protrusions, from right to left, which are obtained at the 10V pulse of 5, 10, 30, 60 and 100s, respectively, and the corresponding height profile is the online of oxide dots; (b)-(d) CNT tip vs. conductive tip for the oxide dots height, aspect ratio and relationships of growth rate-electric field strength.

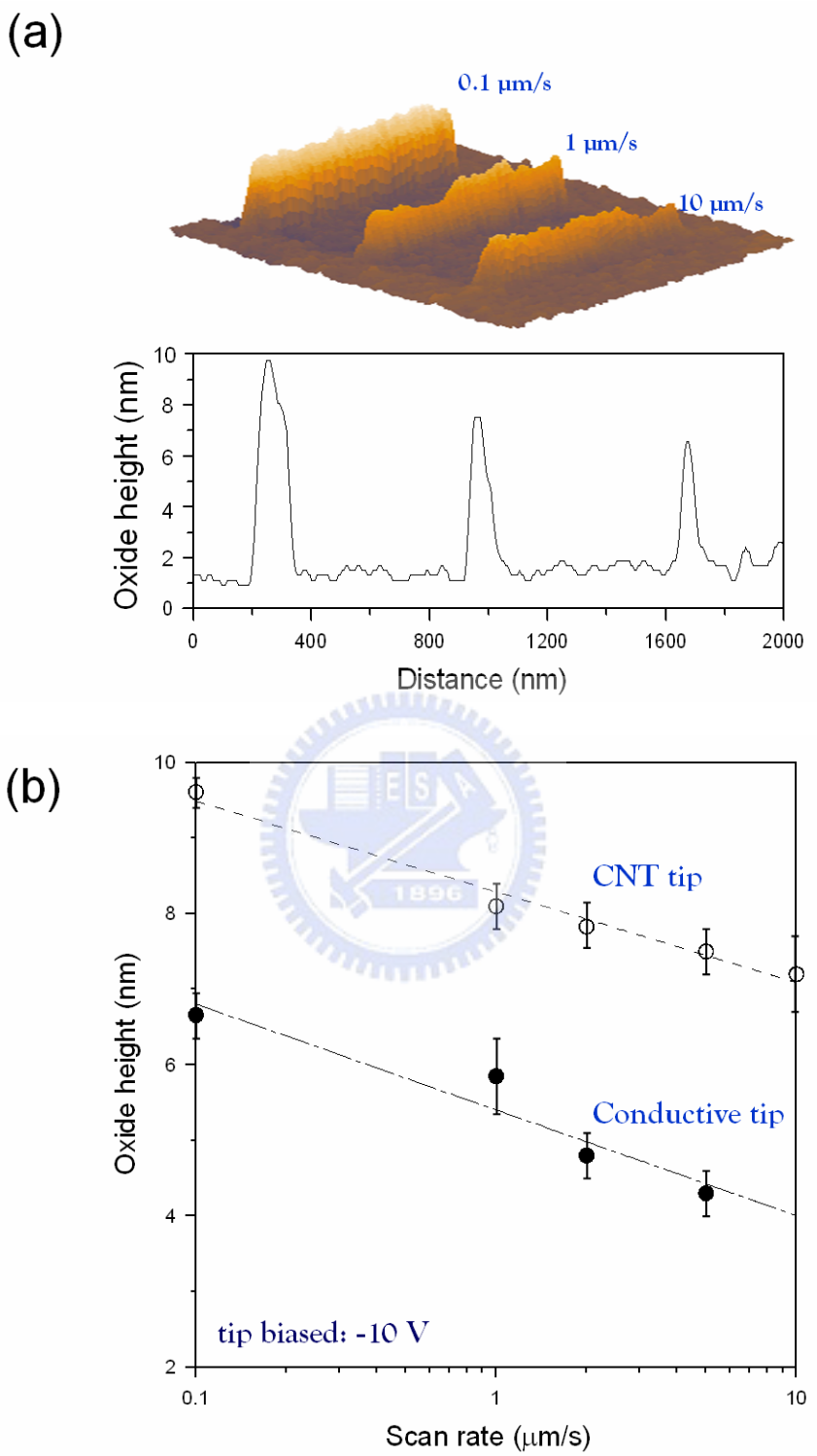

Figure 2-12. (a) AFM image and the height profile of GaAs oxide wires patterned using a scanning rate of 0.1, 1 and 10μm/s at -10V tip bias, respectively; (b) Variation in the height of the oxide vs. the scan rate of the CNT and/ conductive tip.

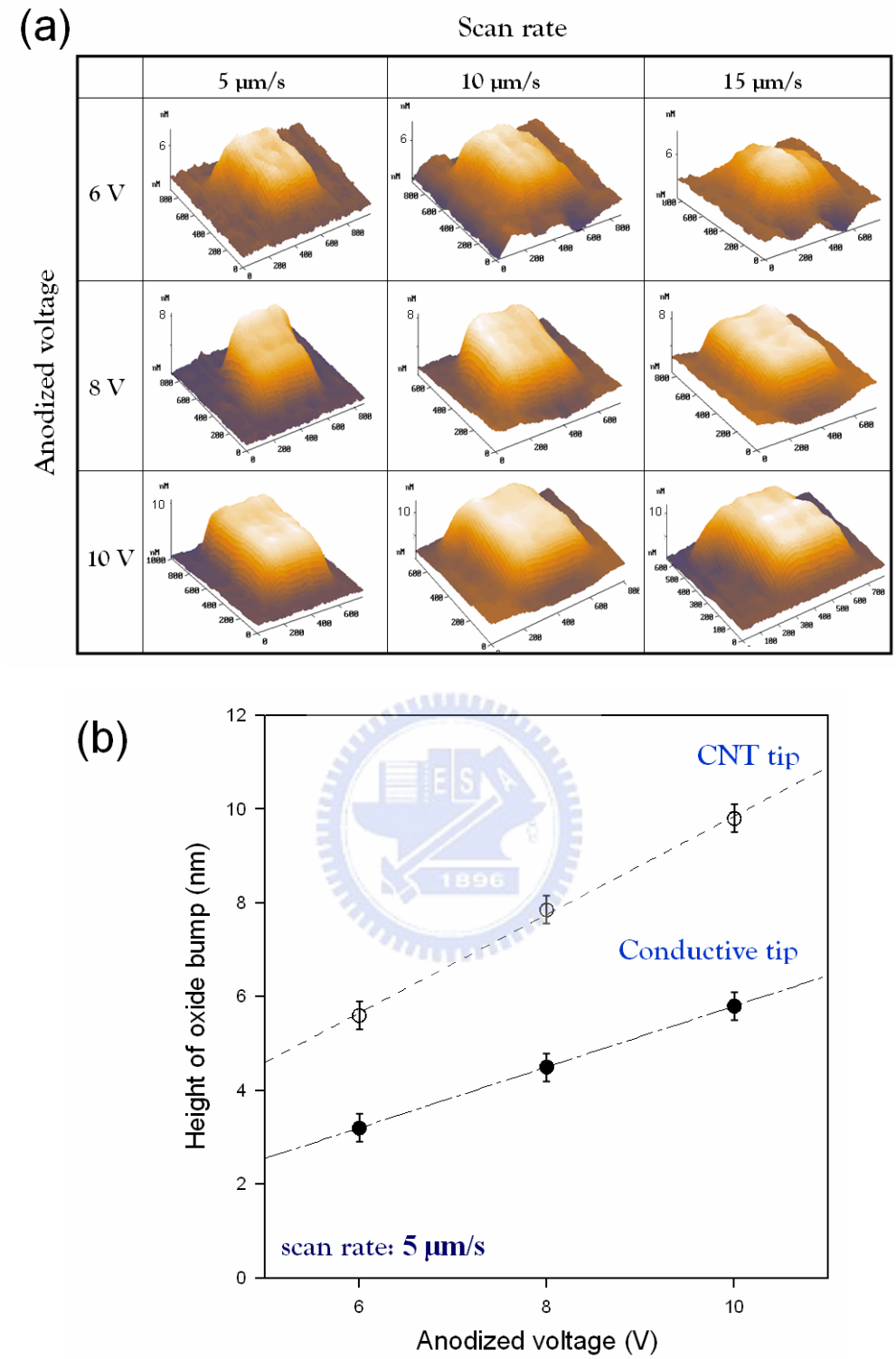

Figure 2-13. (a) An AFM image depicting an array of 9 rectangular oxide bumps on p-GaAs(100) surface; (b) A linear graph of height and sample voltage of both CNT and conductive tips.

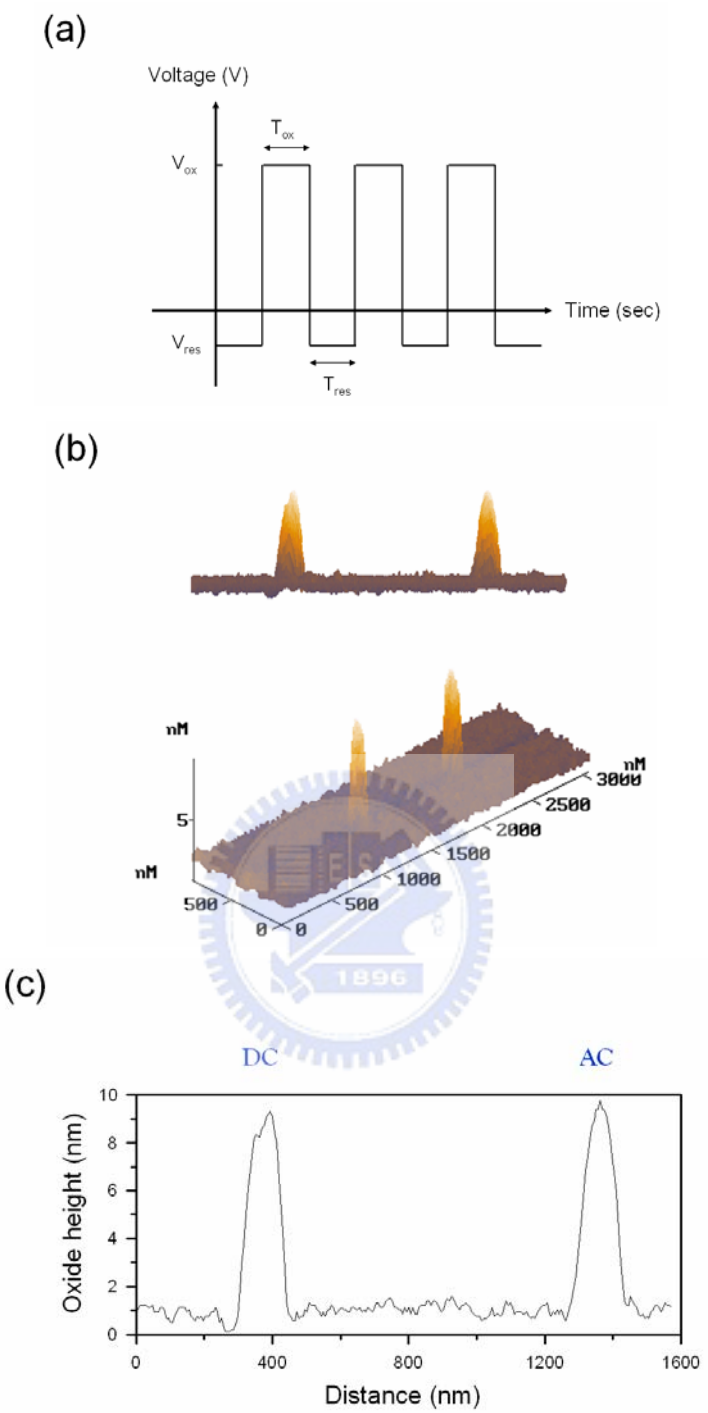

Figure 2-14. (a) Waveform voltage applied to the GaAs surface with respect to the CNT tip when performing an oxidation under AC conditions: T_{ox} is the time as the oxidation is performed (the voltage applied to the sample is V_{ox}), and Tres is the rest time (the voltage applied is V_{res}); (b) 2D and 3D AFM images representation of two fabricated dots, left (DC voltage of 10V) and right (AC voltage, T_{ox}=T_{res}=50ms, V_{ox}=10V, V_{res}=-10V), at the relative humidity of 55% and total time=60s; (c) Height profile of two dots.

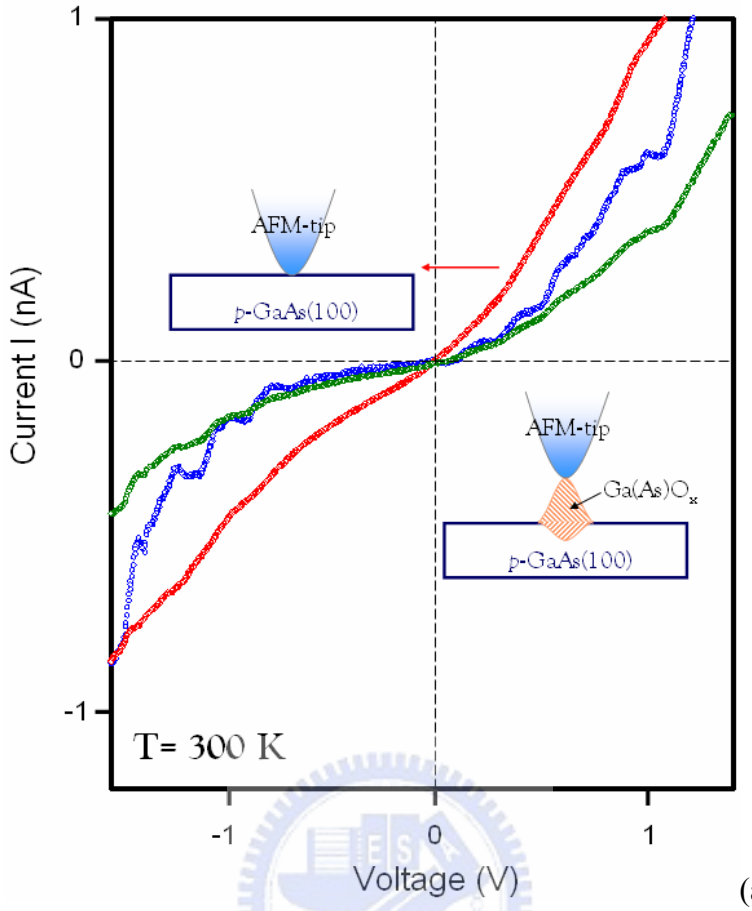

(a)

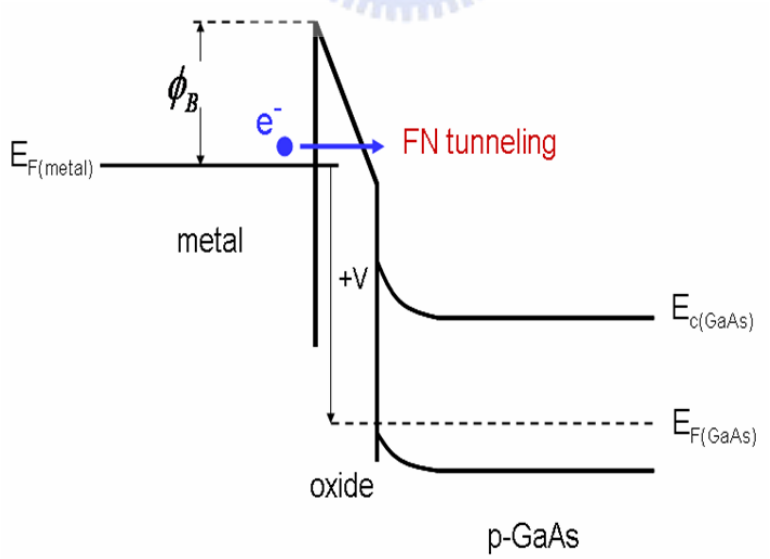

(b)

Figure 2-15. (a) Measured I-V curves for before (red) and after (blue and green) the fabrication of GaAs oxide dots and (b) the energy band diagram for the metal tip/tip-induced Ga(As)Ox/p-GaAs(100) in the Fowler-Nordheim bias range (V>0).

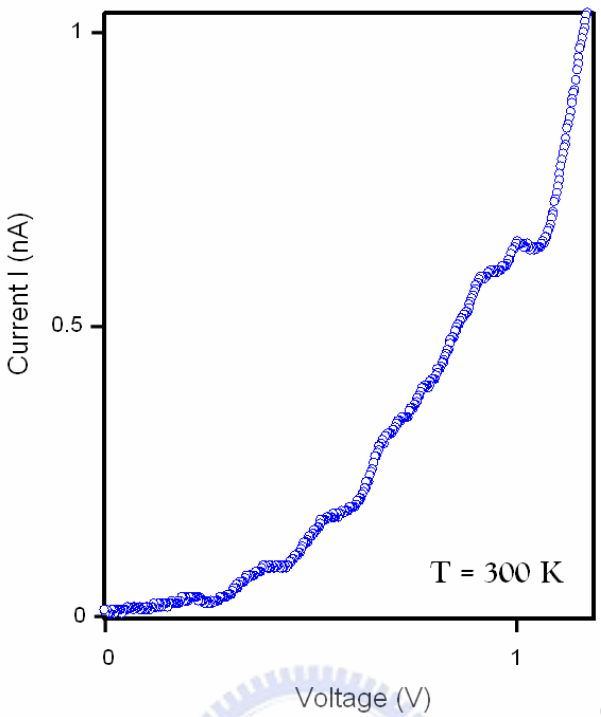

(a)

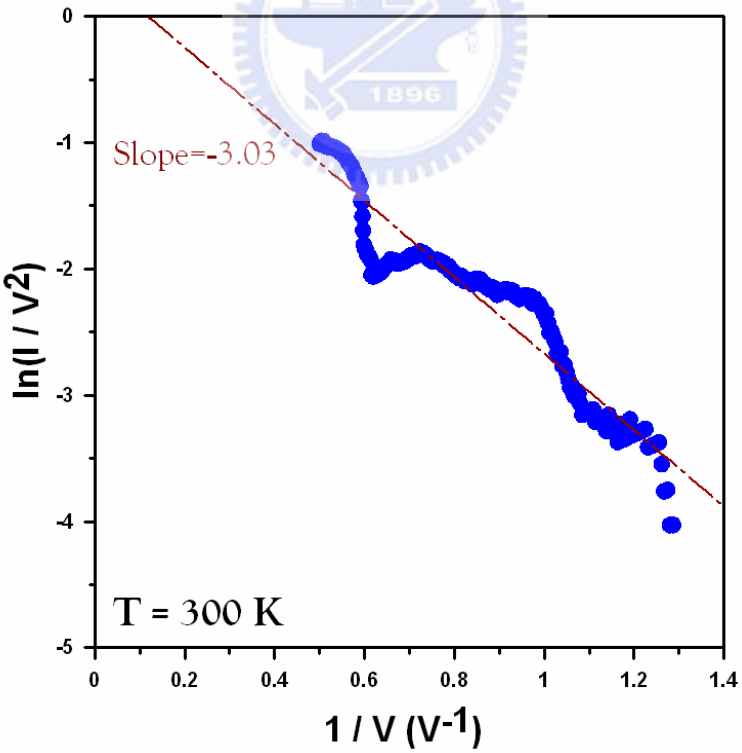

(b)

Figure 2-16. (a) taken I-V curve measured across the GaAs oxide dot from Fig.2-15(a) and, (b) modified Fowler-Nordheim plot of ln(I/V²) versus 1/V.